nature portfolio

Peer Review File

Durable acidic water oxidation ruthenium based electrocatalyst by fluorination induced symmetry breaking

Corresponding Author: Professor Xiaoqing Huang

This file contains all reviewer reports in order by version, followed by all author rebuttals in order by version.

Version 0:

Reviewer comments:

Reviewer #1

(Remarks to the Author)
This work presents a strategy utilizing F-induced symmetry breaking to inhibit structural degradation of RuO_2, achieving 2-month stability under industrial-grade current densities of 1000 mA cm-2. However, the conclusion regarding the switchable reaction mechanism from the LOM to the AEM, driven by the F-doping, lacks sufficient evidence from appropriate control experiments and theoretical calculations. In addition, relevant literatures on anionic doping in RuO2 have not been adequately referenced and compared (B-RuO2, Angew. Chem. Int. Ed. 2024, 63 (50), e202411603, DOI: 10.1002/anie.202411603; Cl-RuO2, Angew. Chem. Int. Ed. 2025, 64, e202420860, DOI: 10.1002/anie.202420860), which makes it difficult to assess the novelty and innovation of this work. Therefore, in its present form, I consider that the manuscript cannot meet the high standards of Nature Communications.

1. The authors claim that RuO2 is widely recognized to follow the LOM mechanism, however, the theoretical calculations of OER activity in RuO2 presented in this work focus solely on the AEM pathway. In other words, the barriers calculated does not correspond to the lowest energy barrier for RuO2-based catalysts. In addition, there is a lack of systematic investigation into the differences in energy barriers between the LOM and AEM pathways in RuO2-based catalysts, as well as the effect of anionic doping.
2. Another point of concern is the authors' statement: "As predicted by DFT, a marked decline in OER activity and stability was observed when O was replaced by S, Se, and P….." (Line 192-193, Page 9). How does the DFT calculation predict stability degradation following the doping of S, P, or Se?
3. The concept of symmetry breaking lacks a clear definition or quantitative indicators. It should not only be supported by theoretical calculations but also validated through experimental evidence. Additionally, doping any element could lead to structural changes in RuO2, making the selection of the dopant particularly crucial. The authors chose S/P/Se as dopants, which belong to different periods and main groups compared to F, raising ambiguity, as it would be more straightforward to compare fluorine with elements from the same period (such as C, N, or B). The extent of symmetry breaking induced by F (which may be insufficient) and S (which may be excessive) could deviate from the optimal range needed for maximum OER activity, suggesting that the actual peak performance might lie in dopant systems not yet explored.
4. The use of carbon support for the PEMWE test is confusing, as carbon supports are inherently unstable under acidic OER conditions, particularly at high potentials. If this material is ever going to be used in an electrolyzer, it should also be possible to use it in an unsupported manner. In addition, it would be beneficial to include characterization of the carbon support after long-term PEMWE testing.
5.The introduction fails to adequately review current modification strategies for RuO2 and lacks a comparison of anion dopants with other alternatives, such as metal dopants, overlooking a critical analysis of how anion dopants can address the existing stability challenges.
6. The absence of in-situ experiments for undoped RuO2 and S/P/Se-doped RuO2 limits the validation of the proposed switchable reaction mechanism, particularly regarding the effects of F doping.
7. The manuscript lacks detailed synthetic protocols for S/P/Se-RuO_2 materials, with some descriptions remaining ambiguous (e.g., "Concurrently, M–RuO2/(F)C...heat treatment process"). Additionally, there is no quantification of noble metal mass loading in any of the electrochemical measurements. These insufficient experimental details hinder the accurate evaluation of the OER performance of the catalysts.

Reviewer #2

(Remarks to the Author)
The manuscript describes the modelling, fabrication, characterization and electrochemical testing of anion doped ruthenium oxide catalysts for oxygen evolution reaction (OER) in acidic electrolyte. The manuscript is well structured and logically organized. The champion fluorine doped ruthenium oxide shows impressive activity and robustness towards OER. The manuscript could be accepted with the following minor aspects having been addressed.
1. As the dopant is essential to break the symmetry and induce electrocatalytic activity, the nature of the dopant is important information. What is the dopant level of the fluorine doped ruthenium oxide and did the author observe any dopant level dependent activity towards OER?
2. There has been debate on the true active site of the anion doped metal oxide as OER electrocatalyst and whether the active site could be preserved after long-term test. It is suggested that the author provide more material characterization data to show the structural properties.
3. To further prove the stability of the electrocatalysts, the leaching of ruthenium from the electrocatalysts with and without dopant can be monitored and compared.
4. Are the identified intermediates in the in-situ IR/Raman spectroscopy characterizations unique to the fluorine doped ruthenium oxide or they are generally observed for ruthenium oxide. The information is useful for the discussion of role of dopant/asymmetry on the reaction mechanism.
5. It is suggested that the scale bars could be added to the images, such as Figure 2d, e, h, i.
6. The experimental details on the fabrication of anion doped ruthenium oxide samples, PEM water electrolyzers, in-situ testing (e.g., Raman spectroscopy), could be provided for the audience.
7. Is it very obvious that the electrocatalyst is iridium–free as no iridium has been used in this work? The authors could consider an alternative manuscript title.
8. The authors should double check the wordings, such as absorb/adsorb, figure numbers.

Reviewer #3

(Remarks to the Author)
In this manuscript, the authors endeavor to markedly enhance the stability of Ru-based catalysts via fluorine doping strategies. However, further supplementation and refinement are required regarding the microscopic mechanism of symmetry breaking, the comprehensiveness of experimental validation, and the depth of comparison with state-of-the-art research. It is recommended that the authors strengthen the correlation between theoretical calculations and experimental characterizations, while clearly articulating the positioning of innovation points within the existing framework to elevate the novelty and persuasiveness of the manuscript.

1. The introduction does not adequately address current approaches to resolving stability issues in ruthenium-based catalysts (e.g., heterometal doping, interface engineering, strain regulation, high-entropy compounds, etc.). Literature searches indicate that these strategies have achieved substantial advancements. It is advised to incorporate relevant references to bolster the comprehensiveness of the discussion.
2. The specific mechanism by which F-induced symmetry breaking suppresses LOM lacks sufficient detail. Existing studies (e.g., 10.1002/anie.202420848, 10.1038/s41467-024-49281-2) demonstrate that lattice symmetry breaking inhibits OLE participation through elongation of Ru-O bond lengths and reduced covalency. Further elucidation of the effects of F doping on electronic structures and reaction pathways using DFT calculations is warranted.
3. In Figure 1, the authors focus solely on the F-RuO2(110) surface without explaining the rationale for selecting this orientation (e.g., exposed crystal surfaces, reactive site distributions). Comparative analysis of other crystal faces (e.g., (100), (111)) is recommended to validate the universality of the findings.
4. In Figure 1, the authors state that F-RuO2 is positioned at the bottom of the volcano inversion diagram; however, the introduction of F only induces a slight symmetry breaking. Further validation is required to confirm whether this conclusion aligns with the simulation results for other halogens (e.g., Cl and Br), thereby avoiding overinterpretation of a single data point. Additionally, more detailed information should be provided to compare the local structural changes in RuO_2 after substitution by different elements (e.g., bond lengths, bond angles).
5. In Figure 1, the authors do not address potential overlooked factors in the DFT simulations (e.g., solvent effects, zero-point energy corrections). It is recommended to include a critical evaluation of the model's assumptions, such as whether the effect of octahedral distortion on oxygen vacancy (OV) formation energy has been overestimated.
6. In Figure 1, the authors briefly describe the mechanism by which F suppresses Ru dissolution (e.g., O-2p band center shift). It is suggested to integrate Bader charge analysis to elucidate how F enhances stability through electronic structure regulation and discuss its applicability under various acidic conditions.
7. In Figures 2-3, the lattice strain mechanism induced by F is insufficiently explained. The interaction between the F-O bond and Ru-O bond should be clarified using DFT calculations.
8. In Figure 3, the Ru valence states predicted by DFT (e.g., average oxidation state reduced to +3.5) should be quantitatively correlated with experimental data (e.g., XPS Ru 3p peak negative shift). The original paper only provides a qualitative description of "electron density adjustment." It is recommended to quantify the polarization effect of F on Ru charge using Bader charge analysis and compare it with relevant experimental characterization results (e.g., XPS and EXAFS).
9. In Figure 4, the authors do not explicitly clarify whether resistance voltage drop (iR) correction has been applied to the overpotential (η). In acidic electrolytes, electrode interface impedance (R_total) may lead to an overestimation of η, particularly when the catalyst exhibits poor conductivity (e.g., RuO_2-based materials).
10. In Figure 4, the author merely claims that "F introduces more active sites," which lacks robust and direct evidence.
11. The comparison between DFT predictions and experimental results remains superficial (e.g., only "symmetry breaking"

is mentioned), and the adsorption energy or reaction pathway of key intermediates has not been quantitatively validated. It is recommended to include in the supplementary material a correlation between the ΔG* (OER steps) calculated via DFT and the Tafel slope measured experimentally to establish a clear theory-experiment mapping.
12. In Figure 5, no explicit correlation mechanism linking F doping with the AEM path has been established, and there is a lack of DFT transition state analysis or EXAFS surface coordination verification.
13. Inferring from XRD structural stability that O does not participate in the reaction involves a logical leap; oxygen isotope tracking data should be incorporated for validation.
14. It is suggested that the conclusion propose additional research directions, such as investigating the impact of other halogens (Cl, Br) or non-elemental doping on symmetry breaking and OER properties, as well as exploring the potential characteristics and performance of the catalyst under reaction conditions.
15. The description of the DFT calculation method omits several critical details, including the model size, whether atoms are fixed, how the adsorption site is determined, and how free energy is calculated and corrected. It is recommended that the authors consult relevant literature to provide a comprehensive description to ensure the reproducibility of the computational results.

Version 1:

Reviewer comments:

Reviewer #1

(Remarks to the Author)
The author provided some new materials in response to my questions, but most of my doubts remain unresolved.
1. First, the concept of symmetry breaking lacks a clear definition, along with quantitative metrics to measure its extent. The authors define symmetry breaking as "the structural modifications at atomic scale that reduce its crystal symmetry". However, this definition remains somewhat generalized and does not provide a clear method for quantifying the degree of symmetry breaking based on experimental evidence. Generally, any elemental doping or substitution will introduce atomic-scale structural modifications, which inherently trigger symmetry breaking.
2. Current experimental evidence confirms the successful doping of elements, such as N, S, P, Se, Cl and Br into RuO2. However, there is no definitive experimental data demonstrating how these dopants specifically change the degree of symmetry breaking.
3. The authors propose that the doping amount of F in RuO2 is controlled by the annealing temperature. However, numerous studies have demonstrated that annealing temperature, even without any elemental doping, can significantly alter the intrinsic structure of RuO2, such as the strength of Ru-O bonds and structural stability. These structural changes, in turn, influence both the catalytic activity and stability (Nat. Commun. 2025, 16, 801, DOI：10.1038/s41467-025-56188-z). Therefore, the approach of using annealing temperature to control the F doping amount lacks sufficient rigor and needs further clarification.
4. The newly added [Page 14, Lines 14–15] states: "Next, the ink was vertically dripped on the glassy carbon electrode (0.196 cm^2) to obtain the work electrode (loading amount: ~75 mg Ru)." The high loading of Ru seems to exaggerate the OER activity. A comparison with previous studies should be provided and summarized.
5. Additional, [Page 14, Lines 9–12]: "In addition, melamine, …… at 450 °C, 150 °C, 300 °C, 500 °C, 450 °C, and 350 °C, respectively". The repetition of 450 °C appears to be an error. Such inconsistencies may undermine the rigor of the manuscript.
6. The PEM tests lack control samples (RuO_2, RuO_2/(F)C) for comparison, which are crucial for enabling readers to more effectively assess the catalytic performance.
In summary, this manuscript does not provide sufficient evidence to demonstrate clear differences in the degree of symmetry breaking across various anionic dopants. Therefore, this work far can not meet the high standards of Nature Communications.

Reviewer #2

(Remarks to the Author)
The authors have addressed the comments in the revised manuscript. The manuscript is now acceptable to the journal.

Reviewer #3

(Remarks to the Author)
The authors considered the suggestions of the reviewers and made comprehensive revisions to the manuscript. I think this manuscript has now met the requirements for publication.

Version 2:

Reviewer comments:

Reviewer #1

(Remarks to the Author)

In the revised manuscript, the authors have made efforts to improve the quality of the presented research. However, the reviewer raises a final concern regarding how to distinguish the effects of doping amount from the type of doping element on the Baur distortion indices.

Version 3:

Reviewer comments:

Reviewer #1

(Remarks to the Author)
The authors have revised the manuscript appropriately. The current version of the manuscript can be accepted for publication.

Responses to Reviewers

Dear Reviewers,

Thank you for your precious time to constructive comments on our manuscript titled **"Ultradurable acidic water oxidation iridium–free electrocatalyst by fluorination induced symmetry–breaking"** (**Manuscript ID: NCOMMS-25-10822**) for ***Nature Communications***. We sincerely appreciate your opinions and confirmation of our work. Accordingly, we have made the corresponding response and revision based on those comments. For other concerns on our work, we have also supplied the corresponding response.

Reviewer #1

General Comment: This work presents a strategy utilizing F–induced symmetry breaking to inhibit structural degradation of RuO_2, achieving 2–month stability under industrial–grade current densities of 1000 mA cm^{-2}. However, the conclusion regarding the switchable reaction mechanism from the LOM to the AEM, driven by the F–doping, lacks sufficient evidence from appropriate control experiments and theoretical calculations. In addition, relevant literatures on anionic doping in RuO_2 have not been adequately referenced and compared (B–RuO_2, Angew. Chem. Int. Ed. 2024, 63 (50), e202411603, DOI: 10.1002/anie.202411603; Cl–RuO_2, Angew. Chem. Int. Ed. 2025, 64, e202420860, DOI: 10.1002/anie.202420860), which makes it difficult to assess the novelty and innovation of this work. Therefore, in its present form, I consider that the manuscript cannot meet the high standards of Nature Communications.

[**Author's Response**]: Thank you very much for your constructive comments. We highly appreciate that you strictly point out our deficiency in this work and we are truly sorry that our work did not supply a satisfying interpretation and explanation to demonstrate our research. By following your suggestions, we rechecked our manuscript and made the corresponding improvement.

In the revised manuscript, we elaborated in detail from both computational and experimental perspectives that the symmetry breaking induced by F leads to the transformation of the OER mechanism from LOM to AEM. The specific description is as follows:

The desirable Gibbs free energy of rate–determining step (RDS) for F–RuO_2 is 1.80 eV, lower than that of S–RuO_2 (1.86 eV), P–RuO_2 (2.60 eV), Se–RuO_2 (2.76 eV), N–RuO_2 (1.83 eV), Cl–RuO_2 (3.16 eV), Br–RuO_2 (4.28 eV) and RuO_2 (1.89 eV) (**Fig. 1c**). Notably, a decrease of the Ru d–band center relative to fermi energy level (E_f) is observed after the partial substitution of O with F, potentially influencing the adsorption/desorption of intermediates on the catalyst surface (**Fig. 1d**).[36] Therefore, compared with the traditional RuO_2 following LOM route, the introduction of F gives RuO_2 more energy advantages on the AEM path (**Supplementary Fig. 20**). **[Page 4, Line 19–21 and Page 5, Line 13–17]**

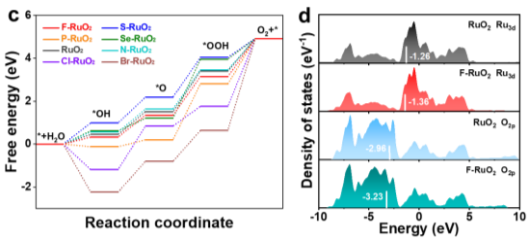

Figure 1. DFT calculations. (**c**) Gibbs free energy diagram for different catalysts. (**d**) DOS of Ru 3d and O 2p for F–RuO_2; corresponding d–band centers are denoted by white lines.

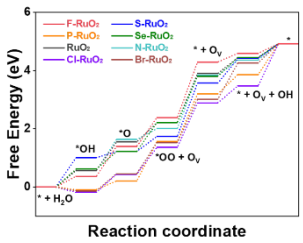

Supplementary Fig. 20. Calculated free energy evolution of OER via LOM on F–RuO_2, S–RuO_2, P–RuO_2, Se–RuO_2, RuO_2, N–RuO_2, Cl–RuO_2 and Br–RuO_2 under electrode potential of 0 V.

As shown in **Fig. 3g–j**, charge density difference and Bader charge analysis also reveals that the valence state of Ru (+1.34) in F–RuO_2 decreases with increasing surrounding electron density, attributing to the electron density surrounding Ru was readjusted as a result of the octahedral symmetry breakdown induced by the highly electronegative F, potentially altering the adsorption of intermediates on RuO_2 and thereby switching the reaction route. **[Page 9, Line 4–8]**

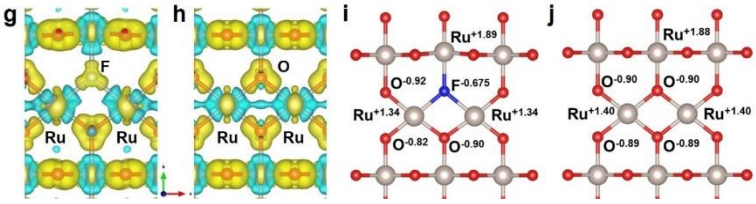

Figure 3. Electronic structure investigation. Electron density difference of (**g**) F–RuO_2/FC and (**h**) RuO_2. The blue and yellow shaded area mean the electron density accumulation and donation and the isosurface value is 0.065 e/Å^3. Bader charge analysis for Ru (grey), F (blue), and O (red) sites of (**i**) F–RuO_2/FC and (**j**) RuO_2.

To investigate the underlying mechanism during the OER process, *in situ* characterizations were conducted in **Fig. 5**. Note of that the diffraction peak intensity does not decrease significantly as the potential range from 1.0 to 1.5 V by *in situ* electrochemical XRD testing, implying the structure of F–RuO_2/FC remain intact during a wide range of potential tests (**Fig. 5a**). More importantly, the well–preserved diffraction peak in the situ monitoring for up to 60 minutes suggests that the O in F–RuO_2/FC may not participate in the OER process, thus deviating from the traditional LOM route (**Supplementary Fig. 68**). **[Page 11, Line 9–15]**

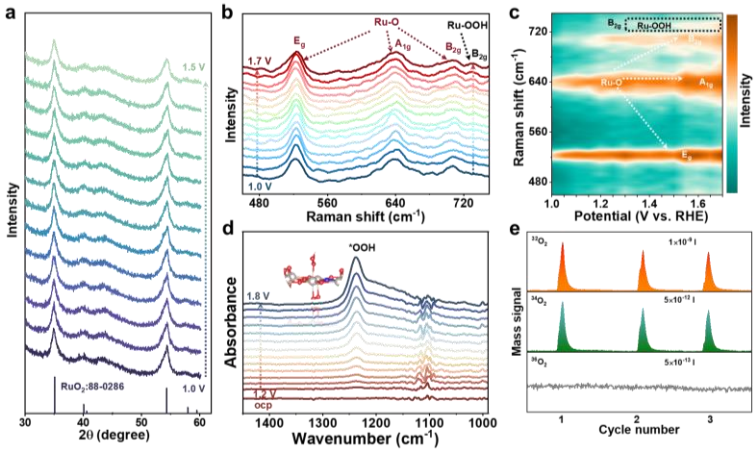

Figure 5. Mechanism explorations. (**a**) In situ XRD patterns, (**b**) *in situ* Raman spectra and (**c**) corresponding contour plots, (**d**) *in situ* ATR–IR spectra of F–RuO_2/FC. (**e**) DEMS signals of $^{32}O_2$, $^{34}O_2$, and $^{36}O_2$ from the gaseous products for ^{18}O–labeled F–RuO_2/FC catalysts in $H_2{}^{16}O$ aqueous H_2SO_4 electrolyte during three times of LSV cycles.

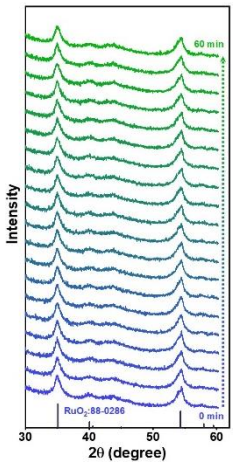

Supplementary Fig. 68. *In situ* XRD patterns of F–RuO_2/FC within 60 min.

To verify this conjecture, the dynamic evolution of the surface structure during the OER process is monitored by *in situ* electrochemical Raman spectroscopy (**Fig. 5b**). Surprisingly, a new Raman peak emerges gradually at ~731 cm^{-1} with the applied potential increases, compared with RuO_2/C, attributed to the formation of Ru–OOH intermediates in the AEM pathway (**Supplementary Fig. 69**).[44] As shown in **Fig. 5c**, the corresponding contour plots exhibit significantly enhanced vibration signals of B_{2g} for Ru–OOH intermediates except for the predominant surface feature signals of Ru–O bonds, proving that the reaction intermediates in the AEM pathway are indeed captured. **[Page 11, Line 18–23]**

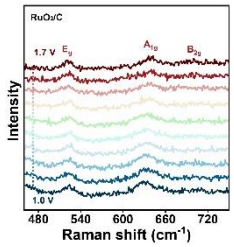

Supplementary Fig. 69. *In situ* Raman spectra of RuO_2/C.

To further elucidate the actual OER route, *in situ* attenuated total reflectance infrared (ATR–IR) spectroscopy was carried out to detect the reaction intermediates. As shown in **Supplementary Fig. 70**, two absorption peaks attributed to the *OO intermediate formed during the LOM pathway are detected, further indicating that RuO_2/C follow the conventional LOM pathway during the acidic OER process.[45] Conversely, *in situ* ATR–IR spectroscopy of F–RuO_2/FC showed a sharp characteristic peak appear at 1237 cm^{-1}, belonging to the stretching vibration of surface–adsorbed *OOH intermediates, evidencing the dominance of the AEM pathway (**Fig. 5d**).[46] Obviously, the signals of *OOH intermediates gradually appear and are significantly enhanced with the increase of potential, indicating that the incorporation of F can force the reaction mechanism of RuO_2 from the traditional LOM to AEM, thus ensuring exceptional stability even at high applied potential. Additionally, F–RuO_2/FC shows clearly pH–independence, suggesting the significant suppression of the LOM pathway and the dominant role of the AEM pathway (**Supplementary Fig. 71**).[47, 48] **[Page 12, Line 1–12]**

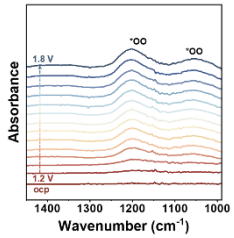

Supplementary Fig. 70. *In situ* ATR–IR spectra of RuO_2/C.

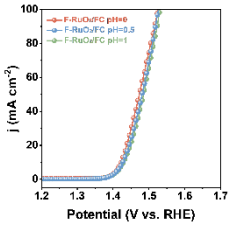

Supplementary Fig. 71. OER polarization curves of F–RuO_2/FC in various pH–H_2SO_4 electrolytes.

Finally, the oxygen isotope tracking experiment was carried out to verify the suppressed LOM process, that is, whether lattice oxygen was involved in the reaction. Operando differential electrochemical mass spectrometry (DEMS) was performed on ^{18}O isotope–labelled F–RuO_2/FC using linear sweep voltammograms (LSV) in $H_2{}^{16}O$ 0.5 M H_2SO_4 (**Supplementary Fig. 73a**). As shown in **Fig. 5e**, the mass signals of $^{32}O_2$ and $^{34}O_2$ were detected without $^{36}O_2$ products, suggesting the non–participation of O_L in the OER process.[50] The mass signals of $^{32}O_2$ gradually increase and present a constant ratio ($^{32}O_2$:$^{34}O_2$) with the occurrence of OER, further demonstrating the dominant AEM pathway (**Supplementary Fig. 73b, c**). **[Page 12, Line 16–21]**

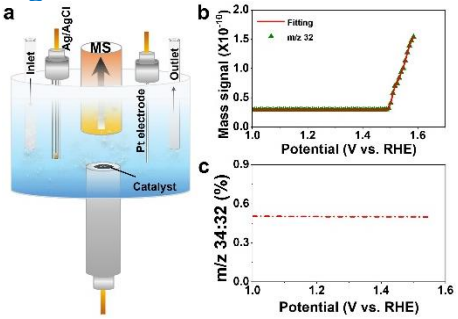

Supplementary Fig. 73. (a) Schematic illustration of the operando DEMS device. (**b**) DEMS signals of $^{32}O_2$ (^{16}O + ^{16}O) were collected during the LSV cycle. (**c**) Ratio of $^{34}O_2$:$^{32}O_2$ within the LSV range.

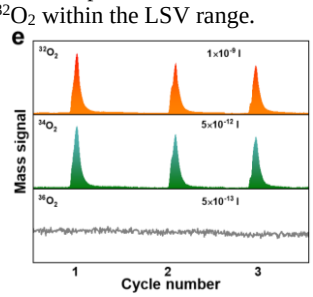

Figure 5. Mechanism explorations. (**e**) DEMS signals of $^{32}O_2$, $^{34}O_2$, and $^{36}O_2$ from the gaseous products for ^{18}O–labeled F–RuO_2/FC catalysts in $H_2{}^{16}O$ aqueous H_2SO_4 electrolyte during three times of LSV cycles.

Based on your suggestions, we have conducted an in–depth discussion on the current modification strategies of RuO_2 (including anion doping) in the introduction part of the revised manuscript and carried out a performance comparison in the performance part, as follows:

As so far, numerous feasible approaches have been reported to significantly enhance the formation energy of O_V, including heterometal doping ($SnRuO_x$[21], Ni–RuO_2[22], Ta_1/RuO_2[23]), interface engineering (Co–Ru@RuO_2 9:1[24], GB–RuO_2[25]), strain regulation ($Li_{0.52}RuO_2$[26], $RuSnO_x$[27]), high–entropy compounds (M–$RuIrFeCoNiO_2$[28]), anion regulation (LD–B/RuO_2[29], Ru/Se–RuO_2[30], RuO_2–Cl[31]) and so on. Among these, the superior electronegativity and electron affinity of anions are more conducive to optimizing the adsorption/desorption behavior of reaction intermediates on the electrocatalyst surface.[32] Nevertheless, most recently reported anion–modulated catalysts for OER have predominantly focused on performance enhancement while neglecting the intrinsic connection between the reaction mechanism and microstructure, which impedes the in–depth understanding of highly efficient electrocatalysts. **[Page 3, Line 5–14]**

[21] Shi, Z. *et al.* Customized reaction route for ruthenium oxide towards stabilized water oxidation in high–performance PEM electrolyzers. *Nat. Commun.* **14**, 843 (2023). **[Page 16, Line 14–15]**

[22] Wu, Z. Y. *et al.* Non–iridium–based electrocatalyst for durable acidic oxygen evolution reaction in proton exchange membrane water electrolysis. *Nat. Mater.* **22**, 100–108 (2023). **[Page 16, Line 16–17]**
[23] Shim, J. *et al.* Atomically dispersed high-valent d^0–metal breaks the activity–stability trade–off in proton exchange membrane water electrolysis. *J. Am. Chem. Soc.* **147**, 16179–16188 (2025). **[Page 16, Line 18–19]**
[24] Chen, J. *et al.* Cobalt–doped Ru@RuO_2 core–shell heterostructure for efficient acidic water oxidation in low–Ru–loading proton exchange membrane water electrolyzers. *J. Am. Chem. Soc.* **147**, 8720–8731 (2025). **[Page 16, Line 20–22]**
[25] He, W. *et al.* Grain–boundary–rich RuO_2 porous nanosheet for efficient and stable acidic water oxidation. *Angew. Chem. Int. Ed.* **63**, e202405798 (2024). **[Page 16, Line 23–24]**
[26] Qin, Y. *et al.* RuO_2 electronic structure and lattice strain dual engineering for enhanced acidic oxygen evolution reaction performance. *Nat. Commun.* **13**, 3784 (2022). **[Page 16, Line 25–26]**
[27] Xu, Y. *et al.* Strain–modulated Ru–O covalency in Ru–Sn oxide enabling efficient and stable water oxidation in acidic solution. *Angew. Chem. Int. Ed.* **136**, e202316029 (2024). **[Page 16, Line 27–28]**
[28] Hu, C. *et al.* Misoriented high–entropy iridium ruthenium oxide for acidic water splitting. *Sci. Adv.* **9**, eadf9144 (2023). **[Page 16, Line 29–30]**
[29] Chen, G. *et al.* A long–range disordered RuO_2 catalyst for highly efficient acidic oxygen evolution electrocatalysis. *Angew. Chem. Int. Ed.* **63**, e202411603 (2024). **[Page 17, Line 1–2]**
[30] Huang, K. *et al.* Ru/Se–RuO_2 composites via controlled selenization strategy for enhanced acidic oxygen evolution. *Adv. Funct. Mater.* **33**, 2211102 (2023). **[Page 17, Line 3–4]**
[31] Chen, J. *et al.* Chloride residues in RuO_2 catalysts enhance its stability and efficiency for acidic oxygen evolution reaction. *Angew. Chem. Int. Ed.* **137**, e202420860 (2025). **[Page 17, Line 5–6]**
[32] Liu, Y. *et al.* Shining light on anion–mixed nanocatalysts for efficient water electrolysis: fundamentals, progress, and perspectives. *Nano–Micro lett.* **14**, 43 (2022). **[Page 17, Line 7–8]**
[36] Li, L. *et al.* Lanthanide–regulating Ru–O covalency optimizes acidic oxygen evolution electrocatalysis. *Nat. Commun.* **15**, 4974 (2024). **[Page 17, Line 15–16]**
[44] Li, W. Q. *et al.* Identification of the molecular pathways of RuO_2 electroreduction by in–situ electrochemical surface–enhanced Raman spectroscopy. *J. Catal.* **400**, 367–371 (2021). **[Page 18, Line 1–2]**
[45] Gou, W. *et al.* Oxygen spillover from RuO_2 to MoO_3 enhances the activity and durability of RuO_2 for acidic oxygen evolution. *Energy Environ. Sci.* **17**, 6755–6765 (2024). **[Page 18, Line 3–4]**
[46] Jin, H. *et al.* Dynamic rhenium dopant boosts ruthenium oxide for durable oxygen evolution. *Nat. Commun.* **14**, 354 (2023). **[Page 18, Line 5–6]**
[47] Shi, Z. *et al.* Confined Ir single sites with triggered lattice oxygen redox: toward boosted and sustained water oxidation catalysis. *Joule* **5**, 2164–2176 (2021). **[Page 18, Line 7–8]**
[48] Wu, L. *et al.* Role of interfacial water in improving the activity and stability of lattice–oxygen–mediated acidic oxygen evolution on RuO_2. *Angew. Chem. Int. Ed.* e202420848 (2025). **[Page 18, Line 9–10]**
[50] Han, X. *et al.* Defect engineering of RuO_2 aerogels for efficient acidic water oxidation. *ACS Mater. Lett.* **6**, 748–7755 (2024). **[Page 18, Line 13–14]**

Apparently, F–RuO_2/FC present a larger current density and longer stability, outperforming most of the recently reported PEM electrocatalysts (**Fig. 4f** and **Table S4**). **[Page 11, Line 5–7]**

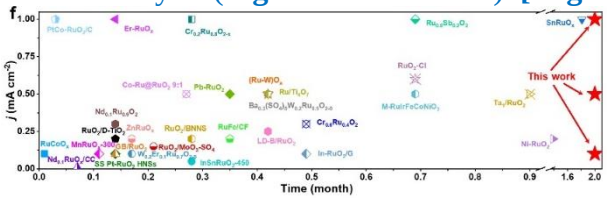

Figure 4. Electrochemical activity studies. (**f**) Comparison of the stability between F–RuO_2/FC and recently reported PEM electrocatalysts.

Table S4. Summary of the reported PEMWE activity and stability using different Ru–based OER electrocatalysts.

Catalyst	Activity (V)	Stability (month)	Ref.
F–RuO_2/FC	**1.45 V@100 mA cm^{-2}**	**2.00@100 mA cm^{-2}**	**This work**
	1.58 V@500 mA cm^{-2}	**2.00@500 mA cm^{-2}**	
	1.70 V@1000 mA cm^{-2}	**2.00@1000 mA cm^{-2}**	
$SnRuO_X$	1.57 V@1000 mA cm^{-2}	1.81@1000 mA cm^{-2}	*Nat. Commun.* **14**, 842 (2023)
Ni–RuO_2	1.78 V@500 mA cm^{-2}	1.39@200 mA cm^{-2}	*Nat. Mater.* **22**, 100–108 (2023)
RuO_2/MoO_3–SO_4	1.75 V@1000 mA cm^{-2}	0.21@150 mA cm^{-2}	*Angew. Chem. Int. Ed.* **63**, e202413653 (2024)
$Nd_{0.1}RuOx$/CC	1.60 V@50 mA cm^{-2}	0.07@10 mA cm^{-2}	*Adv. Funct. Mater.* **33**, 2213304 (2023)
RuO_2/BNNS	/	0.28@200 mA cm^{-2}	*Angew. Chem. Int. Ed.* **136**, e202402018 (2024)
$Nb_{0.1}Ru_{0.9}O_2$	1.69 V@1000 mA cm^{-2}	0.14@300 mA cm^{-2}	*Joule* **7**, 558–573 (2023)
(Ru–W)O_x	1.62 V@1000 mA cm^{-2}	0.42@500 mA cm^{-2}	*Adv. Mater.* **35**, 2305939 (2023)
In–RuO_2/G	/	0.49@100 mA cm^{-2}	*Angew. Chem. Int. Ed.* **136**, e202316903 (2024)
Pb–RuO_2	1.58 V@500 mA cm^{-2}	0.35@500 mA cm^{-2}	*Nat. Commun.* **15**, 9774 (2024)
	1.67 V@1000 mA cm^{-2}		
RuFe/CF	1.90 V@1000 mA cm^{-2}	0.35@200 mA cm^{-2}	*Adv. Mater.* **36**, 2312369 (2024)
$Cr_{0.6}Ru_{0.4}O_2$	1.54 V@1000 mA cm^{-2}	0.49@300 mA cm^{-2}	*J. Am. Chem. Soc.* **146**, 32049–32058 (2024)

$Cr_{0.2}Ru_{0.8}O_{2-x}$	1.77 V@1000 mA cm^{-2}	0.28@1000 mA cm^{-2}	*Nat. Commun.* **15**, 7861 (2024)
$MnRuO_x$–300	1.73 V@500 mA cm^{-2}	0.11@100 mA cm^{-2}	*Angew. Chem. Int. Ed.* **63**, e202405641 (2024)
$Ba_{0.3}(SO_4)_\delta W_{0.2}Ru_{0.5}O_{2-\delta}$	1.54 V@500 mA cm^{-2} 1.68 V@1000 mA cm^{-2}	0.42@500 mA cm^{-2}	*Nat. Commun.* **14**, 8093 (2023)
$RuCoO_x$	1.53 V@100 mA cm^{-2}	0.01@100 mA cm^{-2}	*J. Am. Chem. Soc.* **145**, 17995–18006 (2023)
$InSnRuO_2$–450	1.59 V@100 mA cm^{-2}	0.28@50 mA cm^{-2}	*Adv. Mater.* 2414579 (2024)
$ZnRuO_x$	1.68 V@1000 mA cm^{-2}	0.17@200 mA cm^{-2}	*J. Am. Chem. Soc.* **146**, 15515–15524 (2024)
$W_{0.2}Er_{0.1}Ru_{0.7}O_{2-\delta}$	/	0.17@100 mA cm^{-2}	*Nat. Commun.* **11**, 5368 (2020)
SS Pt–RuO_2 HNSs	/	0.14@100 mA cm^{-2}	*Sci. Adv.* **8**, eabl9271 (2022)
Er–RuO_x	1.59 V@1000 mA cm^{-2}	0.14@1000 mA cm^{-2}	*Nat. Commun.* **15**, 4974 (2024)
$Ru_{0.8}Sb_{0.2}O_2$	1.64 V@1000 mA cm^{-2}	0.69@1000 mA cm^{-2}	*J. Am. Chem. Soc.* **146**, 23146–23157 (2024)
LD–B/RuO_2	1.63 V@1000 mA cm^{-2}	0.42@250 mA cm^{-2}	*Angew. Chem. Int. Ed.* e202411603 (2024)
PtCo–RuO_2/C	2.00 V@4400 mA cm^{-2}	0.03@1000 mA cm^{-2}	*Energy Environ. Sci.* **146**, 1119–1130 (2022)
RuO_2/D–TiO_2	1.74 V@1500 mA cm^{-2}	0.14@200 mA cm^{-2}	*ACS Catal.* **12**, 9437–9445 (2022)
GB/RuO_2	1.54 V@1000 mA cm^{-2}	0.14@100 mA cm^{-2}	*Angew. Chem. Int. Ed.* e202411603 (2024)
Ru/Ti_4O_7	1.69 V@500 mA cm^{-2}	0.42@500 mA cm^{-2}	*Nat. Commun.* **15**, 2728 (2024)
Ta_1/RuO_2	1.80 V@3500 mA cm^{-2}	0.90@500 mA cm^{-2}	*J. Am. Chem. Soc.* **147**, 16179–16188 (2025)
Co–Ru@RuO_2 9:1	1.58 V@1000 mA cm^{-2}	0.27@500 mA cm^{-2}	*J. Am. Chem. Soc.***147**, 8720–8731 (2025)
M–RuIrFeCoNiO_2	/	0.69@500 mA cm^{-2}	*Sci. Adv.* **9**, eadf9144 (2023)
RuO_2–Cl	1.54 V@1000 mA cm^{-2}	0.69@600 mA cm^{-2}	*Angew. Chem. Int. Ed.* **64**, e202420860 (2025)

1. The authors claim that RuO_2 is widely recognized to follow the LOM mechanism, however, the theoretical calculations of OER activity in RuO_2 presented in this work focus solely on the AEM pathway. In other words, the barriers calculated does not correspond to the lowest energy barrier for RuO_2–based catalysts. In addition, there is a lack of systematic investigation into the differences in energy barriers between the LOM and AEM pathways in RuO_2–based catalysts, as well as the effect of anionic doping.

[**Author's Response**]: Thank you for your constructive feedback, which have helped us significantly improve the quality of our manuscript. As requested, M–RuO_2 (M = F, S, Se, P, N, Cl, and Br) was constructed to evaluate their OER performance. The desirable Gibbs free energy of rate–determining step (RDS) for F–RuO_2 is 1.80 eV, lower than that of S–RuO_2 (1.86 eV), P–RuO_2 (2.60 eV), Se–RuO_2 (2.76 eV), N–RuO_2 (1.83 eV), Cl–RuO_2 (3.16 eV), Br–RuO_2 (4.28 eV) and RuO_2 (1.89 eV) (**Fig. 1c**). Compared with the traditional RuO_2 following LOM route, the introduction of F gives RuO_2 more energy advantages on the AEM path (**Supplementary Fig. 20**). Apparently, with the increase of the degree of symmetry–breaking, the energy barriers of RDS in the AEM pathway are elevated and the energy barriers of the RDS in the LOM pathway are decreased, the situation of the OER mechanism is not consistent at different anion doping, and the weaker symmetry breaking is more favorable to the AEM. **[Page 4, Line 19–22 and Page 5, Line 15–17]**

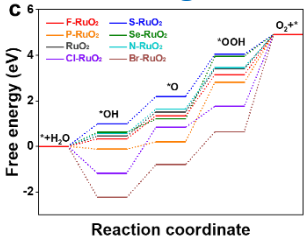

Figure 1. DFT calculations. (**c**) Gibbs free energy diagram for different catalysts.

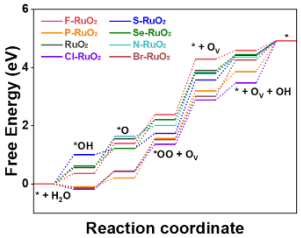

Supplementary Fig. 20. Calculated free energy evolution of OER via LOM on F–RuO_2, S–RuO_2, P–RuO_2, Se–RuO_2, RuO_2, N–RuO_2, Cl–RuO_2 and Br–RuO_2 under electrode potential of 0 V.

2. Another point of concern is the authors' statement: "As predicted by DFT, a marked decline in OER activity and stability was observed when O was replaced by S, Se, and P….." (Line 192-193, Page 9). How does the DFT calculation predict stability degradation following the doping of S, P, or Se?

[**Author's Response**]: We sincerely appreciate your thorough review and insightful comments on our manuscript. In response to your concerns, we have supplemented additional data and revised the manuscript where appropriate, as follows:

As predicted by the DFT, the RDS energy barrier of OER (**Fig. 1c**) and the enthalpy change caused by O loss (**Fig. 1e**) will undergo significant changes when O was replaced by S, Se, P, N, Cl, Br, suggesting that the symmetry–breaking induced by different anions result in varied performance (**Supplementary Fig. 64, 65**). **[Page 4, Line 19–22 and Page 5, Line 23–Page 6, Line 2 and Page 10, Line 16–19]**

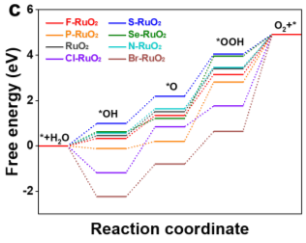

Figure 1. DFT calculations. (**c**) Gibbs free energy diagram for different catalysts.

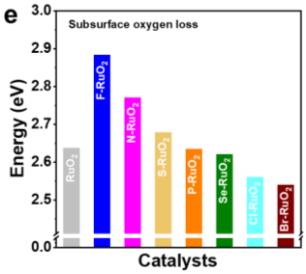

Figure 1. DFT calculations. (**e**) Calculated enthalpy changes for subsurface oxygen loss of various catalysts.

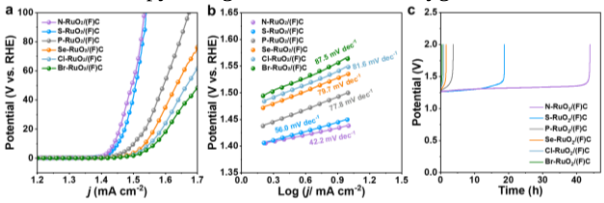

Supplementary Fig. 64. (**a**) OER polarization curves, (**b**) Tafel plots, and (**c**) chronopotentiometry tests of N–RuO_2/(F)C, S–RuO_2/(F)C, P–RuO_2/(F)C, Se–RuO_2/(F)C, Cl–RuO_2/(F)C and Br–RuO_2/(F)C.

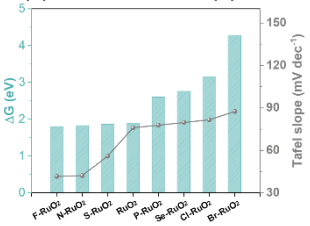

Supplementary Fig. 65. Gibbs free energy of RDS versus Tafel slope.

3. The concept of symmetry breaking lacks a clear definition or quantitative indicators. It should not only be supported by theoretical calculations but also validated through experimental evidence. Additionally, doping any element could lead to structural changes in RuO_2, making the selection of the dopant particularly crucial. The authors chose S/P/Se as dopants, which belong to different periods and main groups compared to F, raising ambiguity, as it would be more straightforward to compare fluorine with elements from the same period (such as C, N, or B). The extent of symmetry breaking induced by F (which may be insufficient) and S (which may be excessive) could deviate from the optimal range needed for maximum OER activity, suggesting that the actual peak performance might lie in dopant systems not yet explored.

[**Author's Response**]: Thank you for your guidance on our manuscript, which help to improve the quality of our work. According to your suggestion, the concept of symmetry–breaking is clearly defined in our revised manuscript, and as follows:

Fundamentally, the intrinsic properties of materials overwhelmingly depend on their crystal symmetry and atomic arrangement. The structural modifications at atomic scale may reduce its crystal symmetry, which is named the symmetry breaking effect.[33–35] **[Page 3, Line 14–16]**

[33] Gao, F. *et al.* Symmetry–breaking induced piezocatalysis of Bi_2S_3 nanorods and boosted by alternating magnetic field. *Appl. Catal. B–Environ.* **316**, 121664 (2022). **[Page 17, Line 9–10]**
[34] Nguyen, Q. N., Wang, C., Shang, Y., Janssen, A. & Xia, Y. Colloidal synthesis of metal nanocrystals: from asymmetrical growth to symmetry breaking. *Chem. Rev.* **123**, 3693–3760 (2023). **[Page 17, Line 11–12]**
[35] Cao, P. *et al.* Breaking symmetry for better catalysis: insights into single–atom catalyst design. *Chem. Soc. Rev.* **54**, 3848–3905 (2025). **[Page 17, Line 13–14]**

To address your concerns, we condected comprehensive characterization of the symmetry breaking of F–RuO_2/FC. The result of analysis revealing that the partial substitution of O by F in RuO_2 leads to symmetry breaking, causing slight distortion of the octahedral configuration and changes in intrinsic properties. The detailed analysis is presented below:

Firstly, to verify the lattice strain mechanism induced by F, long–range ordered atomic arrangements were successfully detected using a spherical AC–HAADF–STEM (**Fig. 2a**). The well–defined lattice spacings (0.22 and 0.18 nm) of (020) and $(21\bar{1})$ planes for RuO_2 unequivocally indicate the presence of lattice strain compared to RuO_2, which may be caused by symmetry breaking due to introduction of heterogeneous atoms (**Fig. 2b**). The fast Fourier transform (FFT) pattern, inset in **Fig. 2b**, reveals the exposed (020) and $(21\bar{1})$ planes along the $[\bar{1}0\bar{2}]$ zone axis of F–RuO_2/FC. To confirm the heterogeneous atoms in F–RuO_2/FC, STEM energy dispersive spectrometer (STEM–EDS) elemental mappings were conducted in **Fig. 2c**. In addition to the uniformly distributed Ru and O elements, conspicuous F signals can be observed, suggesting that the lattice strain in F–RuO_2/FC may be caused by the incorporation of F. **[Page 7, Line 1–11]**

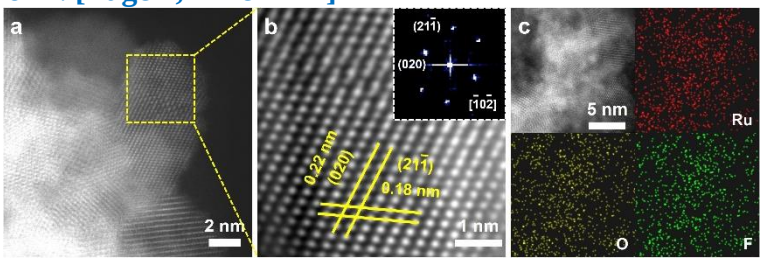

Figure 2. Structural characterizations. (**a**, **b**) spherical aberration–corrected HAADF–STEM images, (**c**) STEM–EDS elemental mappings of F–RuO_2/FC. Inset in (**b**) is the FFT pattern of F–RuO_2/FC.

Secondly, geometrical phase analysis (GPA) was performed to evaluate the strain level and distribution in the F–RuO_2/FC. Evidently, the reduced and enhanced strain can be observed along the horizontal (ε_{xx}) and vertical (ε_{yy}) direction, respectively (**Fig. 2d, e**). The strain profiles of line1 and line2 acquired from strain mappings further confirm that the compressive stress is predominantly along the ε_{xx} direction and the tension stress along the ε_{yy} direction (**Fig. 2f**).[37] **[Page 7, Line 11–15]**

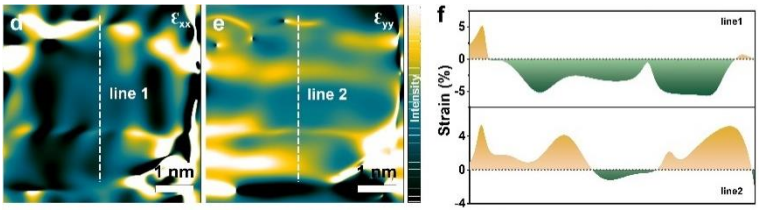

Figure 2. Structural characterizations. Strain mappings of F–RuO_2/FC along (**d**) ε_{xx} and (**e**) ε_{yy} direction from GPA and (**f**) line profiles of strain along the dotted white lines in (**d**) and (**e**).

[37] Wu, G. *et al.* In–plane strain engineering in ultrathin noble metal nanosheets boosts the intrinsic electrocatalytic hydrogen evolution activity. *Nat. Commun.* **13**, 4200 (2022). **[Page 17, Line 17–18]**

Thirdly, to investigate the critical insight of chemical distributions for F–RuO_2/FC, TOF–SIMS analysis was performed in **Fig. 2g**. The element intensity versus sputter time reveals that the concentration of O^- is notably greater than that of Ru^+, being consistent with the characteristics of RuO_2. In addition, the detected RuF^- signals indicate that F indeed replaces part of O and then bonds with Ru during the heat treatment process. Two–dimensional (2D) TOF–SIMS elemental mappings also confirm the presence of significant RuF^- species alongside the abundant Ru and O species (**Fig. 2h**). Clearly, the distribution of Ru and O signals throughout the space in three–dimensional (3D) TOF–SIMS views indicates that the predominant species is RuO_2, consistent with the AC–HAADF–STEM analysis (**Fig. 2i**). The uniform distribution of RuF^- signals throughout the entire 3D space further confirms the partial substitution of O by F, thus leading to the formation of Ru–F bonds. **[Page 7, Line 15–Page 8, Line 2]**

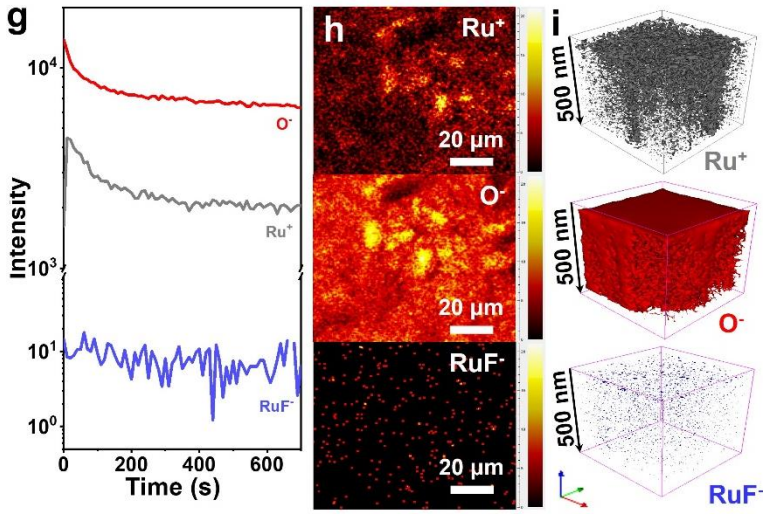

Figure 2. Structural characterizations. (**g**) TOF–SIMS depth analysis of Ru^+, O^-, and RuF^- for F–RuO_2/FC and (**h**) corresponding 2D elemental mapping images and (**i**) 3D render overlay images.

Next, XRD with Rietveld refinement was conducted to obtain the detailed unit cell parameter (**Fig. 2j** and **Table S2**). The sharp diffraction peaks correspond to the tetragonal RuO_2 with the space group *P42/mnm*, indicating that the adsorbed $RuCl_3$ on the surface of FC gradually crystallizes into RuO_2 during the heat treatment process. The presence of Ru accelerates the local pyrolysis of FC and resulting in F occupying part of the position of O in F–RuO_2/FC (inset in **Fig. 2j**). **[Page 8, Line 2–7]**

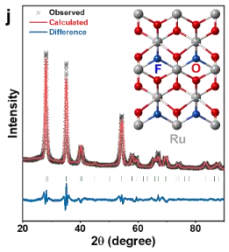

Figure 2. Structural characterizations. (**j**) XRD pattern of F–RuO_2/FC. Inset in (**j**) is structural model of F–RuO_2/FC.

Table S2. Refined parameters of F–RuO_2/FC.

F–RuO_2/FC	X	Y	Z
Ru0	0.500000	0.500000	0.500000
Ru1	0.000000	0.000000	0.000000
O2	0.694330	0.694330	0.000000
O3	0.194330	0.805670	0.500000
O4	0.239972	0.225644	–9.999990
F1	0.805670	0.194330	0.500000
a = 4.5436 Å, b = 4.5436 Å, c = 3.1397 Å, space grpup *P42/mnm*, R_{wp} = 6.12%, R_p = 4.70%, Chi2 = 8.977			

Finally, compared to RuO_2, a noticeable red shift can be observed in the vibration peaks of F–RuO_2/FC, which may be caused by the shortened Ru–O owing to the partial substitution of O by the highly electronegative F (**Fig. 3a**).[39] Therefore, F 1s XPS spectra of F–RuO_2/FC present a wider peak than that of FC, corresponding to the C–F and Ru–F species (**Fig. 3b**). Additionally, O 1s XPS peaks of RuO_2 are located at 529.0, 530.0, and 531.7 eV, corresponding to O_L, O_V, and surface–adsorbed H_2O, respectively (**Fig. 3c**).[40, 41] Evidently, a notable shift of the oxygen species towards higher binding energy can be observed in F–RuO_2/FC due to the presence of high electronegativity F results in an altered electronic interaction between Ru and O.[39] **[Page 8, Line 8–17]**

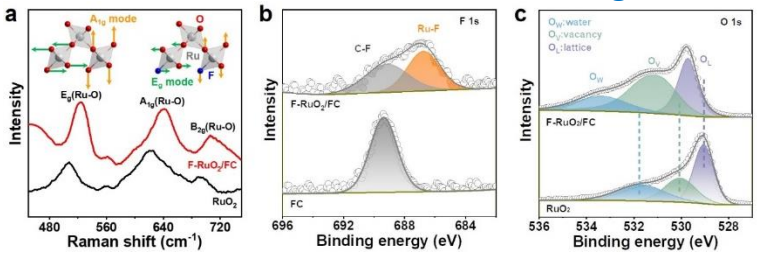

Figure 3. Electronic structure investigation. (**a**) Raman spectra of F–RuO_2/FC and RuO_2. (**b**) F 1s XPS spectra of F–RuO_2/FC and FC. (**c**) O 1s XPS spectra of F–RuO_2/FC and RuO_2.

[39] Xiao, K., Wang, Y., Wu, P., Hou, L. & Liu, Z. Q. Activating lattice oxygen in spinel $ZnCo_2O_4$ through filling oxygen vacancies with fluorine for electrocatalytic oxygen evolution. *Angew. Chem. Int. Ed.* **62**, e202301408 (2023). **[Page 17, Line 21–23]**
[40] Liu, Z. *et al.* Optimal geometrical configuration of cobalt cations in spinel oxides to promote oxygen evolution reaction. *Angew. Chem. Int. Ed.* **59**, 4736–4742 (2020). **[Page 17, Line 24–25]**
[41] Xue, J. Y. *et al.* Engineering multiphasic $MoSe_2$/NiSe heterostructure interfaces for superior hydrogen production electrocatalysis. *Appl. Catal. B–Environ.* **312**, 121434 (2022). **[Page 17, Line 26–27]**

To comprehensively explore the practical peak performance, as requested, N–RuO_2/(F)C electrocatalyst was synthesized using N as dopant (**Supplementary Fig. 58**). Compared to F–RuO_2/FC, the activity and stability of N–RuO_2/(F)C showed markedly reduced, which is consistent with the results predicted by DFT calculation (**Supplementary Fig. 64** and **Fig. 1c, e,** and **f**).

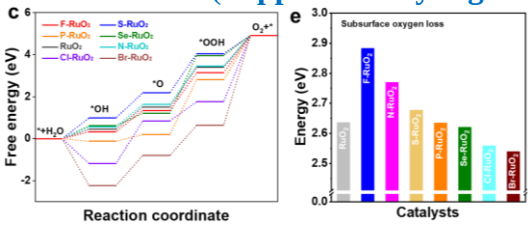

Figure 1. DFT calculations. (**c**) Gibbs free energy diagram for different catalysts. (**e**) Calculated enthalpy changes for subsurface oxygen loss of various catalysts.

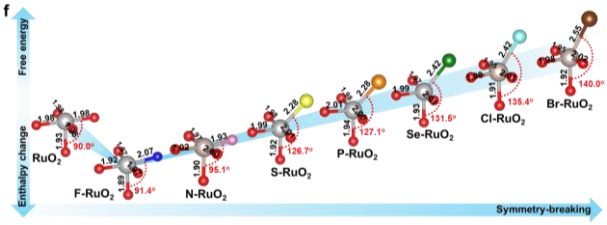

Figure 1. DFT calculations. (**f**) Reaction free energy (RDS) and subsurface O loss enthalpy change volcano against the symmetry–breaking.

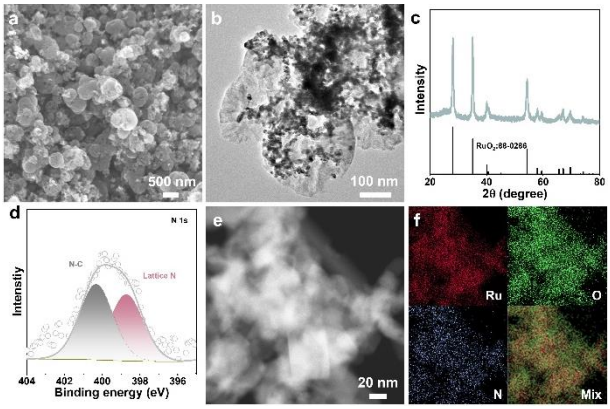

Supplementary Fig. 58. (**a**) SEM image, (**b**) TEM image, (**c**) XRD pattern, (**d**) N 1s XPS spectrum, (**e**) STEM image, and (**f**) STEM–EDS elemental mappings of N–RuO_2/(F)C.

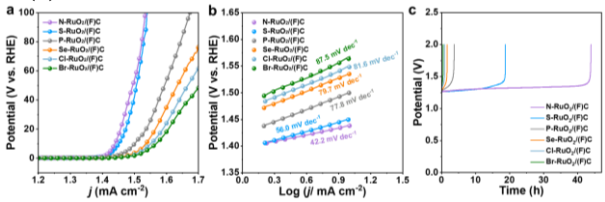

Supplementary Fig. 64. (**a**) OER polarization curves, (**b**) Tafel plots, and (**c**) chronopotentiometry tests of N–RuO_2/(F)C, S–RuO_2/(F)C, P–RuO_2/(F)C, Se–RuO_2/(F)C, Cl–RuO_2/(F)C and Br–RuO_2/(F)C.

4. The use of carbon support for the PEMWE test is confusing, as carbon supports are inherently unstable under acidic OER conditions, particularly at high potentials. If this material is ever going to be used in an electrolyzer, it should also be possible to use it in an unsupported manner. In addition, it would be beneficial to include characterization of the carbon support after long–term PEMWE testing.

[**Author's Response**]: Thank you for the comments. The C–F bond, recognized as one of the strongest single bonds, endows fluorinated materials with high thermal and chemical stability (***Nat. Mater.* 9**, 119–133 (2024)). This unique feature of strong bonding, high electronegativity, and stability makes fluorinated materials widely applicable in the field of energy materials (***Energy Environ. Sci.* 16**, 1907–1942 (2023)).

To investigate the stability of carbon support, the F–RuO_2/FC electrocatalyst after long–term PEMWE test was characterized. The morphology, chemical states, and crystal structure remain largely unchanged, proving exceptional stability (**Supplementary Fig. 66, 67**).[42, 43] **[Page 11, Line 3–5]**

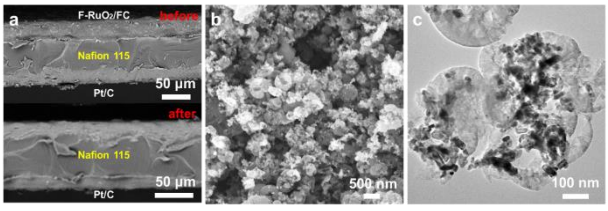

Supplementary Fig. 66. (**a**) SEM images of the cross section of MEA before and after CP test. (**b**) SEM image and (**c**) TEM image of F–RuO_2/FC after CP test of PEMWE.

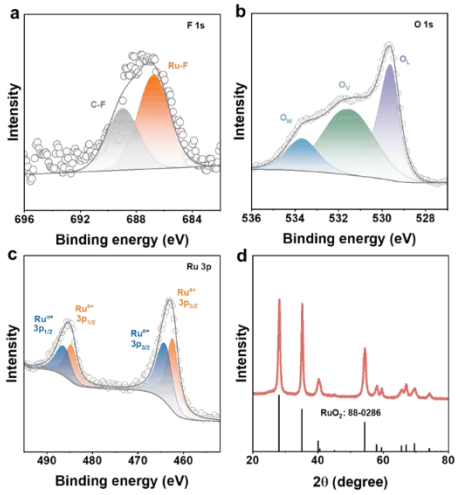

Supplementary Fig. 67. (**a**) F 1s XPS spectrum, (**b**) O 1s XPS spectrum, (**c**) Ru 3p XPS spectrum and (**d**) XRD pattern of F–RuO_2/FC after CP test of PEMWE.

[42] O'Hagan, D. Understanding organofluorine chemistry. an introduction to the C–F bond. *Chem. Soc. Rev.* **37**, 308–319 (2008). **[Page 17, Line 28–29]**
[43] Wang, T. *et al.* Recent advances in fluorine–doped/fluorinated carbon–based materials for supercapacitors. *Energy Storage Mater.* **30**, 367–384 (2020). **[Page 17, Line 30–31]**

5. The introduction fails to adequately review current modification strategies for RuO_2 and lacks a comparison of anion dopants with other alternatives, such as metal dopants, overlooking a critical analysis of how anion dopants can address the existing stability challenges.

[**Author's Response**]: Thanks for your kind suggeation. Based on your consideration, the current modification strategies for RuO_2 and the stability challenges associated with anion doping are thoroughly discussed in the introduction section of our revised manuscript, and as follows:

As so far, numerous feasible approaches have been reported to significantly enhance the formation energy of O_V, including heterometal doping ($SnRuO_x$[21], Ni–RuO_2[22], Ta_1/RuO_2[23]), interface engineering (Co–Ru@RuO_2 9:1[24], GB–RuO_2[25]), strain regulation ($Li_{0.52}RuO_2$[26], $RuSnO_x$[27]), high–entropy compounds (M–$RuIrFeCoNiO_2$[28]), anion regulation (LD–B/RuO_2[29], Ru/Se–RuO_2[30], RuO_2–Cl[31]) and so on. Among these, the superior electronegativity and electron affinity of anions are more conducive to optimizing the adsorption/desorption behavior of reaction intermediates on the electrocatalyst surface.[32] Nevertheless, most recently reported anion–modulated catalysts for OER have predominantly focused on performance enhancement while neglecting the intrinsic connection between the reaction mechanism and microstructure, which impedes the in–depth understanding of highly efficient electrocatalysts. **[Page 3, Line 5–14]**

[21] Shi, Z. *et al.* Customized reaction route for ruthenium oxide towards stabilized water oxidation in high–performance PEM electrolyzers. *Nat. Commun.* **14**, 843 (2023). **[Page 16, Line 14–15]**
[22] Wu, Z. Y. *et al.* Non–iridium–based electrocatalyst for durable acidic oxygen evolution reaction in proton exchange membrane water electrolysis. *Nat. Mater.* **22**, 100–108 (2023). **[Page 16, Line 16–17]**
[23] Shim, J. *et al.* Atomically dispersed high–valent d^0–metal breaks the activity–stability trade–off in proton exchange membrane water electrolysis. *J. Am. Chem. Soc.* **147**, 16179–16188 (2025). **[Page 16, Line 18–19]**
[24] Chen, J. *et al.* Cobalt–doped Ru@RuO_2 core–shell heterostructure for efficient acidic water oxidation in low–Ru–loading proton exchange membrane water electrolyzers. *J. Am. Chem. Soc.* **147**, 8720–8731 (2025). **[Page 16, Line 20–22]**
[25] He, W. *et al.* Grain–boundary–rich RuO_2 porous nanosheet for efficient and stable acidic water oxidation. *Angew. Chem. Int. Ed.* **63**, e202405798 (2024). **[Page 16, Line 23–24]**
[26] Qin, Y. *et al.* RuO_2 electronic structure and lattice strain dual engineering for enhanced acidic oxygen evolution reaction performance. *Nat. Commun.* **13**, 3784 (2022). **[Page 16, Line 25–26]**
[27] Xu, Y. *et al.* Strain–modulated Ru–O covalency in Ru–Sn oxide enabling efficient and stable water oxidation in acidic solution. *Angew. Chem. Int. Ed.* **136**, e202316029 (2024). **[Page 16, Line 27–28]**
[28] Hu, C. *et al.* Misoriented high–entropy iridium ruthenium oxide for acidic water splitting. *Sci. Adv.* **9**, eadf9144 (2023). **[Page 16, Line 29–30]**
[29] Chen, G. *et al.* A long–range disordered RuO_2 catalyst for highly efficient acidic oxygen evolution electrocatalysis. *Angew. Chem. Int. Ed.* **63**, e202411603 (2024). **[Page 17, Line 1–2]**
[30] Huang, K. *et al.* Ru/Se–RuO_2 composites via controlled selenization strategy for enhanced acidic oxygen evolution. *Adv. Funct. Mater.* **33**, 2211102 (2023). **[Page 17, Line 3–4]**

[31] Chen, J. *et al.* Chloride residues in RuO_2 catalysts enhance its stability and efficiency for acidic oxygen evolution reaction. *Angew. Chem. Int. Ed.* **137**, e202420860 (2025). **[Page 17, Line 5–6]**
[32] Liu, Y. *et al.* Shining light on anion–mixed nanocatalysts for efficient water electrolysis: fundamentals, progress, and perspectives. *Nano–Micro lett.* **14**, 43 (2022). **[Page 17, Line 7–8]**

6. The absence of in–situ experiments for undoped RuO_2 and S/P/Se–doped RuO_2 limits the validation of the proposed switchable reaction mechanism, particularly regarding the effects of F doping.
[**Author's Response**]: We deepest gratitude goes to you for your thoughtful suggestion that have helped improve our manuscript substantially. To further investigate the switchable reaction mechanism, *in situ* ATR–IR spectroscopy was performed on RuO_2/C, S–RuO_2/(F)C, P–RuO_2/(F)C and Se–RuO_2/(F)C. As shown in **Supplementary Fig. 70**, two absorption peaks attributed to the *OO intermediate formed during the LOM pathway are detected, further indicating that RuO_2/C follow the conventional LOM pathway during the acidic OER process.[45] **[Page 12, Line 1–4]**

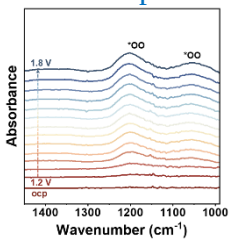

Supplementary Fig. 70. *In situ* ATR–IR spectra of RuO_2/C.

Furthermore, the reaction intermediate signals of *OOH in the AEM pathway and *OO in the LOM pathway were simultaneously detected during the OER process of S–RuO_2/(F)C, but the signals of *OOH are disappeared across the entire potential window of P–RuO_2/(F)C and Se–RuO_2/(F)C (**Supplementary Fig. 72b-d**).[49] Remarkably, *in situ* ATR–IR spectroscopy of F–RuO_2/FC showed a sharp characteristic peak appear at 1237 cm^{-1}, belonging to the stretching vibration of surface–adsorbed *OOH intermediates, evidencing the dominance of the AEM pathway (**Fig. 5d**).[46] Based on the above analysis, it can be concluded that the symmetry breaking in octahedral configuration of RuO_2 induced by different anion dopants enables controllable switching of reaction mechanisms, verifying the feasibility of the symmetry–breaking strategy. **[Page 12, Line 5–7 and Line 12–15]**

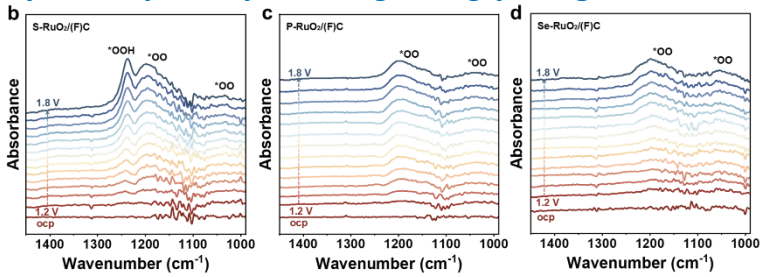

Supplementary Fig. 72. *In situ* ATR–IR spectra of (**b**) S-RuO_2/(F)C, (**c**) P-RuO_2/(F)C, and (**d**) Se-RuO_2/(F)C.

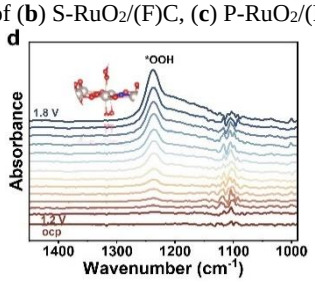

Figure 5. Mechanism explorations. (**d**) *In situ* ATR–IR spectra of F-RuO_2/FC.

[45] Gou, W. *et al.* Oxygen spillover from RuO_2 to MoO_3 enhances the activity and durability of RuO_2 for acidic oxygen evolution. *Energy Environ. Sci.* **17**, 6755–6765 (2024). **[Page 18, Line 3–4]**
[46] Jin, H. *et al.* Dynamic rhenium dopant boosts ruthenium oxide for durable oxygen evolution. *Nat. Commun.* **14**, 354 (2023). **[Page 18, Line 5–6]**
[49] Xu, J. *et al.* $IrO_x \cdot nH_2O$ with lattice water–assisted oxygen exchange for high–performance proton exchange membrane water electrolyzers. *Sci. Adv.* **9**, eadh1718 (2023). **[Page 18, Line 11–12]**

7. The manuscript lacks detailed synthetic protocols for S/P/Se-RuO_2 materials, with some descriptions remaining ambiguous (e.g., "Concurrently, M–RuO_2/(F)C...heat treatment process"). Additionally, there is no quantification of noble metal mass loading in any of the electrochemical measurements. These insufficient experimental details hinder the accurate evaluation of the OER performance of the catalysts.

[**Author's Response**]: Thank you for your careful review of our manuscript. we have provided a detailed description of the synthesis process of M–RuO_2 and the loading of noble metal during the testing process as follows:

Preparation of RuO_2/(F)C. The synthesis condition of RuO_2/(F)C is the same as F–RuO_2/FC, except that the FC used for RuO_2/(F)C was pre–annealed in air at 400 °C for 12 h to remove F (denoted as (F)C). **[Page 14, Line 3–4]**

Preparation of M–RuO_2/(F)C (M = N, S, P, Se, Cl and Br). The M–RuO_2/(F)C electrocatalyst was synthesized by vapor transport method, where the anion–donating powder and RuO_2/(F)C (mass ratio 1:2) were placed at the upstream and downstream positions of a quartz tube, respectively. The anion–donating powder and RuO_2/(F)C were heated to the target temperature and 400 °C respectively at a heating rate of 5 °C min^{-1} in an Ar atmosphere and maintained for 1 h to obtain M–RuO_2/(F)C. In addition, melamine, sulfur powder, sodium hypophosphite, selenium powder, a mixture of polyvinyl chlorid and manganese dioxide, and hexabromobenzene were unsed as anion sources, releasing anions under heat treatment at 450 °C, 150 °C, 300 °C, 500 °C, 450 °C, and 350 °C, respectively. **[Page 14, Line 5–12]**

Electrochemical measurements. Then 2.0 mg of catalyst was added into the solution containing 195 μL of isopropyl alcohol and 5 μL of Nafion, and the ink was prepared by ultrasonic at ambient temperature. Next, the ink was vertically dripped on the glassy carbon electrode (0.196 cm^2) to obtain the work electrode (loading amount: ~75 mg_{Ru}). **[Page 14, Line 14–17]**

PEMWE tests. After ultrasonication for 1 h, the prepared ink were spray onto the both sides of Nafion 115 membrane to get the catalyst–coated membrane (CCM), achieveing noble matal loadings of 2 mg cm^{-2} for anode and 0.5 mg cm^{-2} for cathode. **[Supplementary Information Page 3, Line 1–4]**

Reviewer #2

General Comment: The manuscript describes the modelling, fabrication, characterization and electrochemical testing of anion doped ruthenium oxide catalysts for oxygen evolution reaction (OER) in acidic electrolyte. The manuscript is well structured and logically organized. The champion fluorine doped ruthenium oxide shows impressive activity and robustness towards OER. The manuscript could be accepted with the following minor aspects having been addressed.

[**Author's Response**]: We thank you for the highly positive recommendation. We especially appreciate your comments and advices, which help us to further improve the quality of our work. According to your suggestions, we have carefully revised our manuscript.

1. As the dopant is essential to break the symmetry and induce electrocatalytic activity, the nature of the dopant is important information. What is the dopant level of the fluorine doped ruthenium oxide and did the author observe any dopant level dependent activity towards OER?

[**Author's Response**]: Thanks you for your valuable suggestions. Based on your considerations, the content of F in F–RuO_2/FC was characterized by SEM–EDS. Apparently, the content of F in F–RuO_2/FC varies with the calcination temperature (**Supplementary Fig. 48**), and the lower OER

activity and stability demonstrate its sensitivity to the fluorine doping level (**Supplementary Fig. 50**). **[Page 10, Line 8–10]**

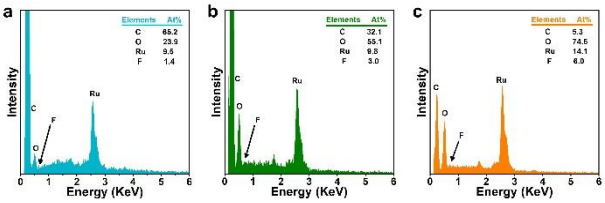

Supplementary Fig. 48. SEM–EDS spectra of (**a**) F–RuO_2/FC–300 °C, (**b**) F–RuO_2/FC, and (**c**) F–RuO_2/FC–500 °C.

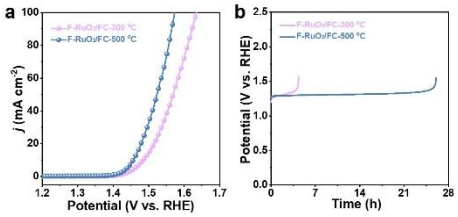

Supplementary Fig. 50. (**a**) OER polarization curves and (**b**) chronopotentiometry tests of F–RuO_2/FC–300 °C and F–RuO_2/FC–500 °C.

2. There has been debate on the true active site of the anion doped metal oxide as OER electrocatalyst and whether the active site could be preserved after long–term test. It is suggested that the author provide more material characterization data to show the structural properties.

[**Author's Response**]: Thanks very much for your insightful comment. We have fully considered your question, and explain as follows:

The flat polarization curve and fleeting stability prove that FC is inert for OER (**Supplementary Fig. 43**). It is noteworthy that the activity and stability are closely resemble that of RuO_2 when it is mechanically mixed with FC, confirming that the unequivocally demonstrates that the F–modified Ru consititutes the true active sites (**Supplementary Fig. 44, 45**). **[Page 10, Line 5–8]**

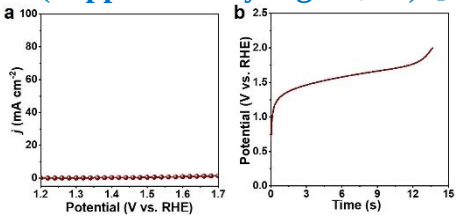

Supplementary Fig. 43. (**a**) OER polarization curve and (**b**) chronopotentiometry test of FC.

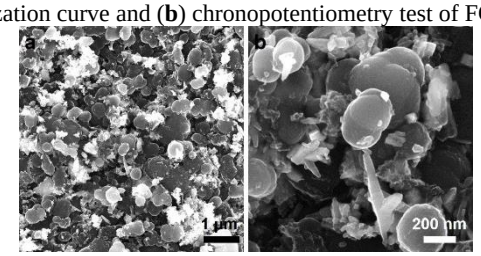

Supplementary Fig. 44. (**a**, **b**) SEM images of RuO_2+FC.

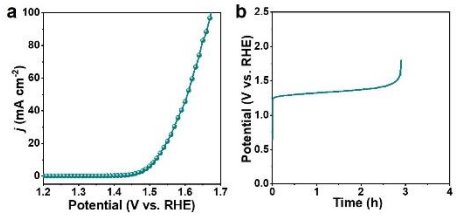

Supplementary Fig. 45. (**a**) OER polarization curve and (**b**) chronopotentiometry test of RuO_2+FC.

Next, the F elements were removed by calcining the FC at 400 °C for 12 h (denoted as (F)C). The sharply reduced activity and stability of RuO_2/(F)C prove that F is decisive for improving the OER performance of RuO_2 (**Supplementary Fig. 55–57**). **[Page 10, Line 12–14]**

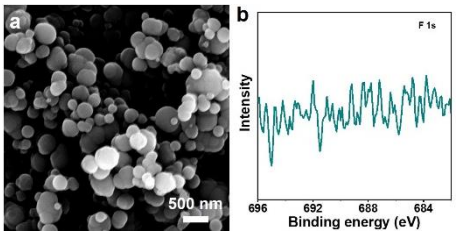

Supplementary Fig. 55. (**a**) SEM image and (**b**) F 1s XPS spectrum of (F)C.

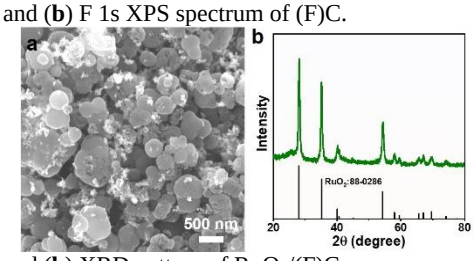

Supplementary Fig. 56. (**a**) SEM image and (**b**) XRD pattern of RuO_2/(F)C.

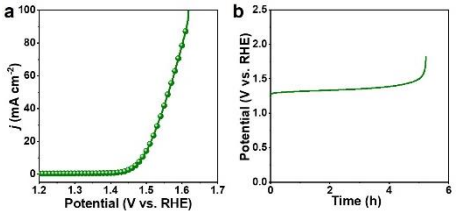

Supplementary Fig. 57. (**a**) OER polarization curve and (**b**) chronopotentiometry test of RuO_2/(F)C.

Importantly, the signal of Ru–F species remained detectable in the F 1s XPS spectra of F–RuO_2/FC after long–term testing, coupled with negligible changes in both crystalline structure and surface chemical states, which confirms the complete preservation of active sites as well as the excellent OER stability of F–RuO_2/FC electrocatalyst (**Supplementary Fig. 66, 67**). **[Page 11, Line 3–5]**

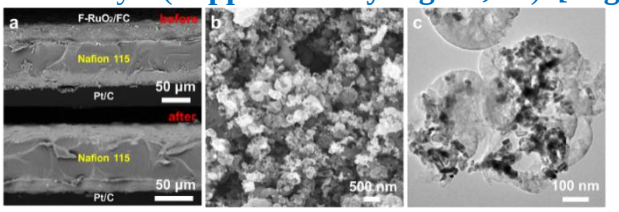

Supplementary Fig. 66. (**a**) SEM images of the cross section of MEA before and after CP test. (**b**) SEM image and (**c**) TEM image of F–RuO_2/FC after CP test of PEMWE.

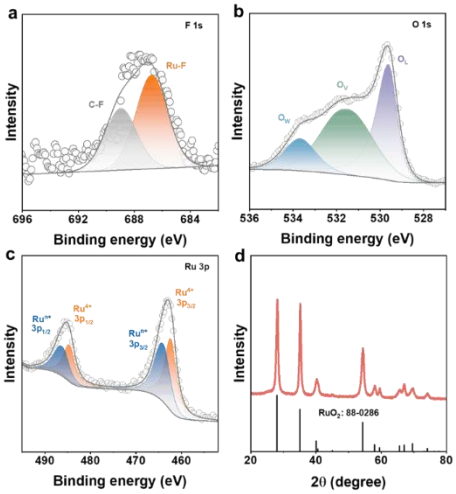

Supplementary Fig. 67. (**a**) F 1s XPS spectrum, (**b**) O 1s XPS spectrum, (**c**) Ru 3p XPS spectrum and (**d**) XRD pattern of F–RuO_2/FC after CP test of PEMWE.

3. To further prove the stability of the electrocatalysts, the leaching of ruthenium from the electrocatalysts with and without dopant can be monitored and compared.

[**Author's Response**]: Thank you very much for your professional comment. As your proposal, a time tracking experiment was performed to monitor the dissolution of Ru in the stability test (**Supplementary Fig. 42**). Surprisingly, F–RuO_2/FC can operate continuously for over 60 h with slightly dissolution of Ru, indicating that the partial substitution of O by F in RuO_2 can significantly improve stability even under harsh acidic conditions. **[Page 10, Line 2–5]**

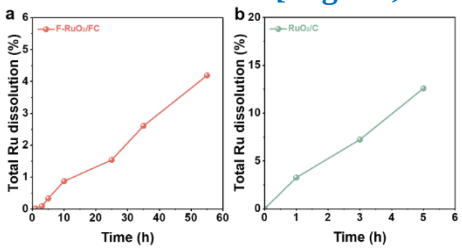

Supplementary Fig. 42. The total Ru dissolution in the electrolyte during chronopotentiometry test of (**a**) F–RuO_2/FC and (**b**) RuO_2/C.

4. Are the identified intermediates in the in–situ IR/Raman spectroscopy characterizations unique to the fluorine doped ruthenium oxide or they are generally observed for ruthenium oxide. The information is useful for the discussion of role of dopant/asymmetry on the reaction mechanism.

[**Author's Response**] Thank you for underlining the deficiency. To address your concern, *in situ* characterizations were performed on RuO_2/C. Obviously, the Raman spectra of RuO_2/C showed no vibration signals of Ru–OOH intermediates, and the distinct stretching vibration of the *OO intermediate were detected in *in situ* ATR–IR spectroscopy, suggesting the RuO_2/C follow the LOM pathway during the OER process (**Supplementary Fig. 69, 70**). **[Page 11, Line 18–21 and Page 12, Line 2–4]**

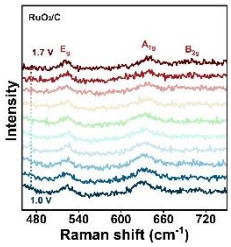

Supplementary Fig. 69. *In situ* Raman spectra of RuO_2/C.

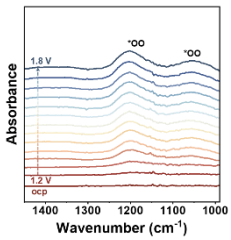

Supplementary Fig. 70. *In situ* ATR–IR spectra of RuO_2/C.

5. It is suggested that the scale bars could be added to the images, such as Figure 2d, e, h, i.

[**Author's Response**]: Thanks you for your detailed review and feedback. According to your suggeation, the scale bars have been added to the Figure 2d, e, h and i in our revised manuscript.

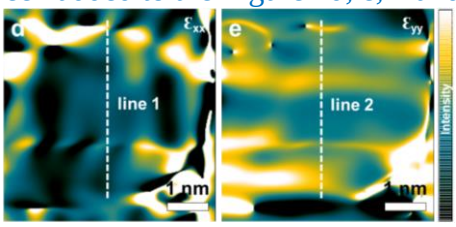

Figure 2. Structural characterizations. Strain mappings of F–RuO_2/FC along (**d**) ε_{xx} and (**e**) ε_{yy} direction from GPA.

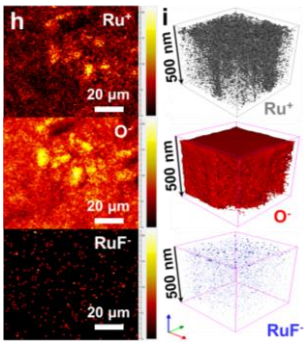

Figure 2. Structural characterizations. TOF–SIMS depth analysis of (**h**) corresponding 2D elemental mapping images and (**i**) 3D render overlay images.

6. The experimental details on the fabrication of anion doped ruthenium oxide samples, PEM water electrolyzers, in–situ testing (e.g., Raman spectroscopy), could be provided for the audience.

[**Author's Response**]: Thanks for your constructive suggeation. As suggested, we have described in detail the synthesis process, PEMWE tests, and *in situ* Raman tests of M–RuO_2 in the experimental section as follows:

Preparation of RuO_2/(F)C. The synthesis condition of RuO_2/(F)C is the same as F–RuO_2/FC, except that the FC used for RuO_2/(F)C was pre–annealed in air at 400 °C for 12 h to remove F (denoted as (F)C). **[Page 14, Line 3–4]**

Preparation of M–RuO_2/(F)C (M = N, S, P, Se, Cl and Br). The M–RuO_2/(F)C electrocatalyst was synthesized by vapor transport method, where the anion–donating powder and RuO_2/(F)C (mass ratio 1:2) were placed at the upstream and downstream positions of a quartz tube, respectively. The anion–donating powder and RuO_2/(F)C were heated to the target temperature and 400 °C respectively at a heating rate of 5 °C min^{-1} in an Ar atmosphere and maintained for 1 h to obtain M–RuO_2/(F)C. In addition, melamine, sulfur powder, sodium hypophosphite, selenium powder, a mixture of polyvinyl chlorid and manganese dioxide, and hexabromobenzene were unsed as anion sources, releasing anions under heat treatment at 450 °C, 150 °C, 300 °C, 500 °C, 450 °C, and 350 °C, respectively. **[Page 14, Line 5–12]**

PEMWE tests. The membrane electrode assembly (MEA) was obtained by Nafion 115 with a geometric area of 1 × 1 cm^2. Commercial Pt/C (20 wt%) and F–RuO_2/FC were used as the cathode and anode, respectively. To prepare anode and cathode ink, the catalysts were dispersed into the solution containing isopropyl alcohol and deionized water with a volume ratio of 2:1, and then the Nafion ionomer (5 wt%) was added (25 wt% relative to both F–RuO_2/FC and Pt/C). After ultrasonication for 1 h, the prepared ink were spray onto the both sides of Nafion 115 membrane to get the catalyst–coated membrane (CCM), achieveing noble matal loadings of 2 mg cm^{-2} for anode and 0.5 mg cm^{-2} for cathode. Subsequently, the CCM was sandwiched between porous Pt–plated Ti foam gas diffusion layer (GDL) and assembled into the PEM cell. Last, 5 N m torque was applied on PEM cell for sealing. During the tests, the PEM cell was operated at 80 °C to obtain polarization curve. The stability of F–RuO_2/FC was evaluated by chronopotentiometry at current density of 100, 500 and 1000 mA cm^{-2}. **[Supplementary Information Page 2, Line 35–Page 3, Line 7]**

***In situ* Raman tests.** A Renishaw InVia Raman spectrometer equipped with 532 nm laser and 50× objective was employed for *in situ* electrochemical Raman measurements. The experiments were conducted in a professionally customized *in situ* Raman reaction cell with a standard three–electrode setup, where the catalyst–coated L–shaped Au gold, Pt wire, and Ag/AgCl electrode were used as the working electrode, counter electrode, and reference electrode, respectively. The *in situ* Raman spectra were ultimately collected while applying a constant potential to the working electrode within the potential range from 1.0 to 1.7 V vs. RHE. **[Supplementary Information Page 2, Line 28–34]**

7. Is it very obvious that the electrocatalyst is iridium–free as no iridium has been used in this work? The authors could consider an alternative manuscript title.
[**Author's Response**]: Thanks for the valuable suggestion. Based on your suggestions, we have revised the title to "**Ultradurable acidic water oxidation ruthenium–based electrocatalyst by fluorination induced symmetry–breaking**" in the revised version. **[Page 1, Line 1–2]**

8. The authors should double check the wordings, such as absorb/adsorb, figure numbers.
[**Author's Response**]: Thank you for your careful checks, we feel sorry for our carelessness. We have thoroughly checked the wording throughout the manuscript, which confirmed that the correct terms are used in the appropriate context and ensured that all figure numbers are accurate and consistent.

Reviewer #3
General Comment: In this manuscript, the authors endeavor to markedly enhance the stability of Ru–based catalysts via fluorine doping strategies. However, further supplementation and refinement are required regarding the microscopic mechanism of symmetry breaking, the comprehensiveness of experimental validation, and the depth of comparison with state–of–the–art research. It is recommended that the authors strengthen the correlation between theoretical calculations and experimental characterizations, while clearly articulating the positioning of innovation points within the existing framework to elevate the novelty and persuasiveness of the manuscript.
[**Author's Response**]: Thank you for the kind support of our work. Your comments have been very helpful for us to further improve the quality of our work. According to your comments, we have made the necessary revision of the manuscript. We hope that the revised manuscript will address all your comments on this work.

1. The introduction does not adequately address current approaches to resolving stability issues in ruthenium–based catalysts (e.g., heterometal doping, interface engineering, strain regulation, high–entropy compounds, etc.). Literature searches indicate that these strategies have achieved substantial advancements. It is advised to incorporate relevant references to bolster the comprehensiveness of the discussion.
[**Author's Response**]: Thanks for your valuable suggestions. Based on your consideration, we have comprehensively discussed currently available feasible strategies for addressing the stability of ruthenium–based catalysts in our revised manuscript, and as follows:

As so far, numerous feasible approaches have been reported to significantly enhance the formation energy of O_V, including heterometal doping ($SnRuO_x$[21], Ni–RuO_2[22], Ta_1/RuO_2[23]), interface engineering (Co–Ru@RuO_2 9:1[24], GB–RuO_2[25]), strain regulation ($Li_{0.52}RuO_2$[26], $RuSnO_x$[27]), high–entropy compounds (M–$RuIrFeCoNiO_2$[28]), anion regulation (LD–B/RuO_2[29], Ru/Se–RuO_2[30], RuO_2–Cl[31]) and so on. Among these, the superior electronegativity and electron affinity of anions are more conducive to optimizing the adsorption/desorption behavior of reaction intermediates on the electrocatalyst surface.[32] **[Page 3, Line 5–11]**

[21] Shi, Z. *et al.* Customized reaction route for ruthenium oxide towards stabilized water oxidation in high–performance PEM electrolyzers. *Nat. Commun.* **14**, 843 (2023). **[Page 16, Line 14–15]**
[22] Wu, Z. Y. *et al.* Non–iridium–based electrocatalyst for durable acidic oxygen evolution reaction in proton exchange membrane water electrolysis. *Nat. Mater.* **22**, 100–108 (2023). **[Page 16, Line 16–17]**
[23] Shim, J. *et al.* Atomically dispersed high–valent d^0–metal breaks the activity–stability trade–off in proton exchange membrane water electrolysis. *J. Am. Chem. Soc.* **147**, 16179–16188 (2025). **[Page 16, Line 18–19]**
[24] Chen, J. *et al.* Cobalt–doped Ru@RuO_2 core–shell heterostructure for efficient acidic water oxidation in low–Ru–loading proton exchange membrane water electrolyzers. *J. Am. Chem. Soc.* **147**, 8720–8731 (2025). **[Page 16, Line 20–22]**

[25] He, W. *et al.* Grain–boundary–rich RuO_2 porous nanosheet for efficient and stable acidic water oxidation. *Angew. Chem. Int. Ed.* **63**, e202405798 (2024). **[Page 16, Line 23–24]**
[26] Qin, Y. *et al.* RuO_2 electronic structure and lattice strain dual engineering for enhanced acidic oxygen evolution reaction performance. *Nat. Commun.* **13**, 3784 (2022). **[Page 16, Line 25–26]**
[27] Xu, Y. *et al.* Strain–modulated Ru–O covalency in Ru–Sn oxide enabling efficient and stable water oxidation in acidic solution. *Angew. Chem. Int. Ed.* **136**, e202316029 (2024). **[Page 16, Line 27–28]**
[28] Hu, C. *et al.* Misoriented high–entropy iridium ruthenium oxide for acidic water splitting. *Sci. Adv.* **9**, eadf9144 (2023). **[Page 16, Line 29–30]**
[29] Chen, G. et al. A long–range disordered RuO_2 catalyst for highly efficient acidic oxygen evolution electrocatalysis. *Angew. Chem. Int. Ed.* **63**, e202411603 (2024). **[Page 17, Line 1–2]**
[30] Huang, K. *et al.* Ru/Se–RuO_2 composites via controlled selenization strategy for enhanced acidic oxygen evolution. *Adv. Funct. Mater.* **33**, 2211102 (2023). **[Page 17, Line 3–4]**
[31] Chen, J. *et al.* Chloride residues in RuO_2 catalysts enhance its stability and efficiency for acidic oxygen evolution reaction. *Angew. Chem. Int. Ed.* **137**, e202420860 (2025). **[Page 17, Line 5–6]**
[32] Liu, Y. *et al.* Shining light on anion–mixed nanocatalysts for efficient water electrolysis: fundamentals, progress, and perspectives. *Nano–Micro lett.* **14**, 43 (2022). **[Page 17, Line 7–8]**

2. The specific mechanism by which F–induced symmetry breaking suppresses LOM lacks sufficient detail. Existing studies (e.g., 10.1002/anie.202420848, 10.1038/s41467-024-49281-2) demonstrate that lattice symmetry breaking inhibits OLE participation through elongation of Ru–O bond lengths and reduced covalency. Further elucidation of the effects of F doping on electronic structures and reaction pathways using DFT calculations is warranted.

[**Author's Response**]: We appreciate your expert suggestions, which will contribute to the refinement of our work. In the revised manuscript, we elucidate the details of the F–induced symmetry breaking suppression of LOM from both computational and experimental perspectives. Meanwhile, the effects of F doping on electronic structures and reaction pathways was further clarified using DFT calculations. The specific description is as follows:

The desirable Gibbs free energy of rate–determining step (RDS) for F–RuO_2 is 1.80 eV, lower than that of S–RuO_2 (1.86 eV), P–RuO_2 (2.60 eV), Se–RuO_2 (2.76 eV), N–RuO_2 (1.83 eV), Cl–RuO_2 (3.16 eV), Br–RuO_2 (4.28 eV) and RuO_2 (1.89 eV) (**Fig. 1c**). Notably, a decrease of the Ru d–band center relative to fermi energy level (E_f) is observed after the partial substitution of O with F, potentially influencing the adsorption/desorption of intermediates on the catalyst surface (**Fig. 1d**).[36] Therefore, compared with the traditional RuO_2 following LOM route, the introduction of F gives RuO_2 more energy advantages on the AEM path (**Supplementary Fig. 20**). **[Page 4, Line 19–22 and Page 5, Line 13–17]**

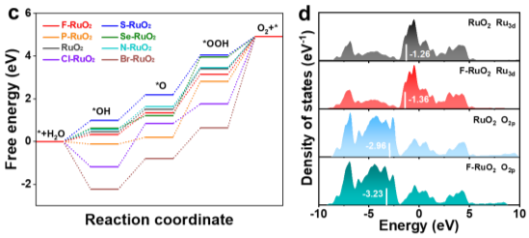

Figure 1. DFT calculations. (**c**) Gibbs free energy diagram for different catalysts. (**d**) DOS of Ru 3d and O 2p for F–RuO_2; corresponding d–band centers are denoted by white lines.

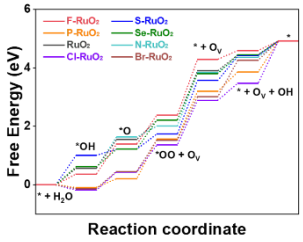

Supplementary Fig. 20. Calculated free energy evolution of OER via LOM on F–RuO_2, S–RuO_2, P–RuO_2, Se–RuO_2, RuO_2, N–RuO_2, Cl–RuO_2 and Br–RuO_2 under electrode potential of 0 V.

As shown in **Fig. 3g–j**, charge density difference and Bader charge analysis also reveals that the valence state of Ru (+1.34) in F–RuO_2 decreases with increasing surrounding electron density,

attributing to the electron density surrounding Ru was readjusted as a result of the octahedral symmetry breakdown induced by the highly electronegative F, potentially altering the adsorption of intermediates on RuO_2 and thereby switching the reaction route. **[Page 9, Line 4–8]**

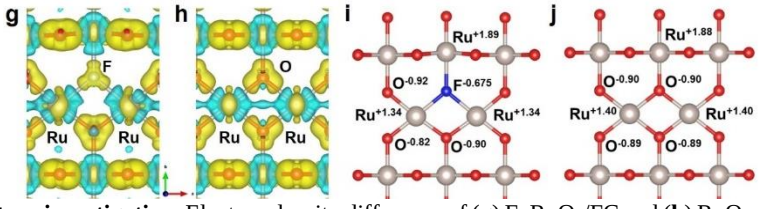

Figure 3. Electronic structure investigation. Electron density difference of (**g**) F–RuO_2/FC and (**h**) RuO_2. The blue and yellow shaded area mean the electron density accumulation and donation and the isosurface value is 0.065 e/Å^3. Bader charge analysis for Ru (grey), F (blue), and O (red) sites of (**i**) F–RuO_2/FC and (**j**) RuO_2.

To investigate the underlying mechanism during the OER process, *in situ* characterizations were conducted in **Fig. 5**. Note of that the diffraction peak intensity does not decrease significantly as the potential range from 1.0 to 1.5 V by *in situ* electrochemical XRD testing, implying the structure of F–RuO_2/FC remains intact during a wide range of potential tests (**Fig. 5a**). More importantly, the well–preserved diffraction peak in the situ monitoring for up to 60 minutes suggests that the O in F–RuO_2/FC may not participate in the OER process, thus deviating from the traditional LOM route (**Supplementary Fig. 68**). **[Page 11, Line 9–15]**

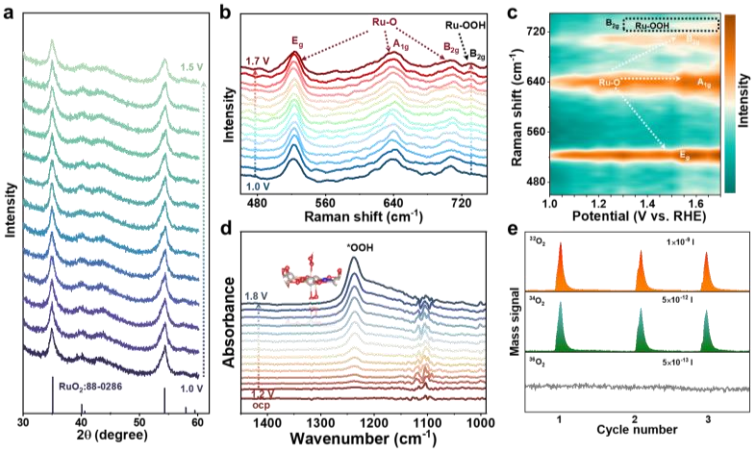

Figure 5. Mechanism explorations. (**a**) In situ XRD patterns, (**b**) *in situ* Raman spectra and (**c**) corresponding contour plots, (**d**) *in situ* ATR–IR spectra of F–RuO_2/FC. (**e**) DEMS signals of $^{32}O_2$, $^{34}O_2$, and $^{36}O_2$ from the gaseous products for ^{18}O–labeled F–RuO_2/FC catalysts in $H_2{}^{16}O$ aqueous H_2SO_4 electrolyte during three times of LSV cycles.

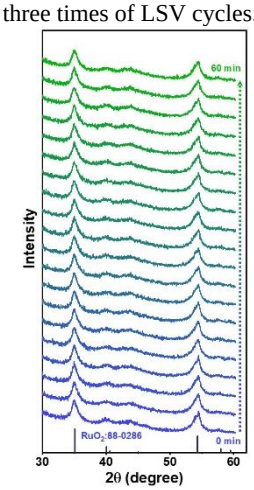

Supplementary Fig. 68. *In situ* XRD patterns of F–RuO_2/FC within 60 min.

To verify this conjecture, the dynamic evolution of the surface structure during the OER process is monitored by *in situ* electrochemical Raman spectroscopy (**Fig. 5b**). Surprisingly, a new Raman peak emerges gradually at ~731 cm^{-1} with the applied potential increases, compared with RuO_2/C,

attributed to the formation of Ru–OOH intermediates in the AEM pathway (**Supplementary Fig. 69**).[44] As shown in **Fig. 5c**, the corresponding contour plots exhibit significantly enhanced vibration signals of B_{2g} for Ru–OOH intermediates except for the predominant surface feature signals of Ru–O bonds, proving that the reaction intermediates in the AEM pathway are indeed captured. **[Page 11, Line 18–23]**

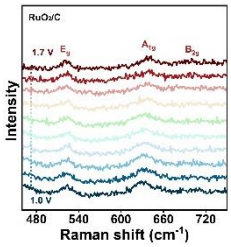

Supplementary Fig. 69. *In situ* Raman spectra of RuO_2/C.

To further elucidate the actual OER route, *in situ* attenuated total reflectance infrared (ATR–IR) spectroscopy was carried out to detect the reaction intermediates. As shown in **Supplementary Fig. 70**, two absorption peaks attributed to the *OO intermediate formed during the LOM pathway are detected, further indicating that RuO_2/C follow the conventional LOM pathway during the acidic OER process.[45] Conversely, *in situ* ATR–IR spectroscopy of F–RuO_2/FC showed a sharp characteristic peak appear at 1237 cm^{-1}, belonging to the stretching vibration of surface–adsorbed *OOH intermediates, evidencing the dominance of the AEM pathway (**Fig. 5d**).[46] Obviously, the signals of *OOH intermediates gradually appear and are significantly enhanced with the increase of potential, indicating that the incorporation of F can force the reaction mechanism of RuO_2 from the traditional LOM to AEM, thus ensuring exceptional stability even at high applied potential. Additionally, F–RuO_2/FC shows clearly pH–independence, suggesting the significant suppression of the LOM pathway and the dominant role of the AEM pathway (**Supplementary Fig. 71**).[47, 48] **[Page 12, Line 1–12]**

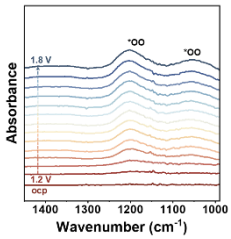

Supplementary Fig. 70. *In situ* ATR–IR spectra of RuO_2/C.

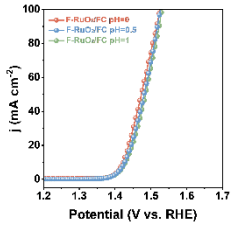

Supplementary Fig. 71. OER polarization curves of F–RuO_2/FC in various pH–H_2SO_4 electrolytes.

Finally, the oxygen isotope tracking experiment was carried out to verify the suppressed LOM process, that is, whether lattice oxygen was involved in the reaction. Operando differential electrochemical mass spectrometry (DEMS) was performed on ^{18}O isotope–labelled F–RuO_2/FC using linear sweep voltammograms (LSV) in $H_2{}^{16}O$ 0.5 M H_2SO_4 (**Supplementary Fig. 73a**). As shown in **Fig. 5e**, the mass signals of $^{32}O_2$ and $^{34}O_2$ were detected without $^{36}O_2$ products, suggesting the non–participation of O_L in the OER process.[50] The mass signals of $^{32}O_2$ gradually increase and present a constant ratio ($^{32}O_2$:$^{34}O_2$) with the occurrence of OER, further demonstrating the dominant AEM pathway (**Supplementary Fig. 73b, c**). **[Page 12, Line 16–21]**

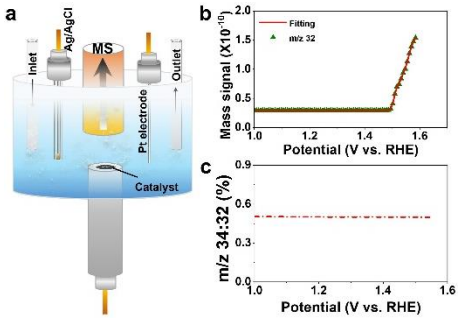

Supplementary Fig. 73. (**a**) Schematic illustration of the operando DEMS device. (**b**) DEMS signals of $^{32}O_2$ (^{16}O + ^{16}O) were collected during the LSV cycle. (**c**) Ratio of $^{34}O_2$:$^{32}O_2$ within the LSV range.

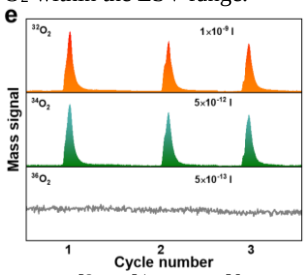

Figure 5. Mechanism explorations. (**e**) DEMS signals of $^{32}O_2$, $^{34}O_2$, and $^{36}O_2$ from the gaseous products for ^{18}O–labeled F–RuO_2/FC catalysts in $H_2{}^{16}O$ aqueous H_2SO_4 electrolyte during three times of LSV cycles.

[36] Li, L. *et al.* Lanthanide–regulating Ru–O covalency optimizes acidic oxygen evolution electrocatalysis. *Nat. Commun.* **15**, 4974 (2024). **[Page 17, Line 15–16]**
[44] Li, W. Q. *et al.* Identification of the molecular pathways of RuO_2 electroreduction by in–situ electrochemical surface–enhanced Raman spectroscopy. *J. Catal.* **400**, 367–371 (2021). **[Page 18, Line 1–2]**
[45] Gou, W. *et al.* Oxygen spillover from RuO_2 to MoO_3 enhances the activity and durability of RuO_2 for acidic oxygen evolution. *Energy Environ. Sci.* **17**, 6755–6765 (2024). **[Page 18, Line 3–4]**
[46] Jin, H. *et al.* Dynamic rhenium dopant boosts ruthenium oxide for durable oxygen evolution. *Nat. Commun.* **14**, 354 (2023). **[Page 18, Line 5–6]**
[47] Shi, Z. et al. Confined Ir single sites with triggered lattice oxygen redox: toward boosted and sustained water oxidation catalysis. *Joule* **5**, 2164–2176 (2021). **[Page 18, Line 7–8]**
[48] Wu, L. *et al.* Role of interfacial water in improving the activity and stability of lattice–oxygen–mediated acidic oxygen evolution on RuO_2. *Angew. Chem. Int. Ed.* e202420848 (2025). **[Page 18, Line 9–10]**
[50] Han, X. *et al.* Defect engineering of RuO_2 aerogels for efficient acidic water oxidation. *ACS Mater. Lett.* **6**, 748–7755 (2024). **[Page 18, Line 13–14]**

3. In Figure 1, the authors focus solely on the F–RuO_2(110) surface without explaining the rationale for selecting this orientation (e.g., exposed crystal surfaces, reactive site distributions). Comparative analysis of other crystal faces (e.g., (100), (111)) is recommended to validate the universality of the findings.

[**Author's Response**]: Thanks for your kind suggestion. The RuO_2(110) facet was selected because it exposes fully coordinated bridged Ru sites and coordination unsaturated sites with quintuple coordination that bind to triple–coordinated oxygen for better identification of the active site.[4-6] Additionally, this surface is known to exhibit the most favorable thermodynamic free energy during most synthesis processes, as established in prior studies.[7] **[Supplementary Information Page 3, Line 11–15]**

As requested, AEM and LOM pathway on different planes ((111) and (100)) of F–RuO_2 and RuO_2 were carried out in **Supplementary Fig. 21**. Apparently, similar phenomena have been observed on different planes ((111) and (100)) of F–RuO_2 and RuO_2, proving its universality. **[Page 5, Line 17–19]**

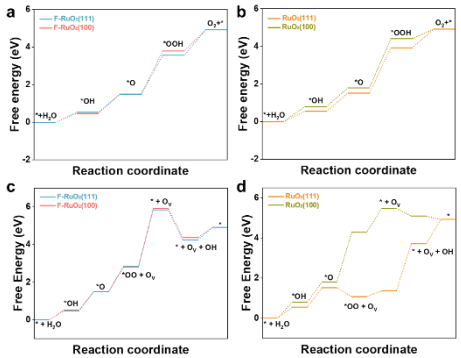

Supplementary Fig. 21. Calculated Gibbs free energy evolution of OER via (**a**, **b**) AEM and (**c**, **d**) LOM on (**a**, **c**) F–RuO_2 and (**b**, **d**) RuO_2.

[4] Sun, Q. *et al.* Effect of a humid environment on the surface structure of RuO_2(110). *Phys. Rev. B* **67**, 205424 (2003). **[Supplementary Information Page 82, Line 7–8]**

[5] Abbott, D. F. *et al.* Oxygen reduction on nanocrystalline ruthenia–local structure effects. *RSC Adv.* 5, 1235–1243 (2014). **[Supplementary Information Page 82, Line 9–10]**

[6] Rao, R. R. *et al.* Operando identification of site–dependent water oxidation activity on ruthenium dioxide single–crystal surfaces. *Nat. Catal.* **3**, 516–525 (2020). **[Supplementary Information Page 82, Line 11–12]**

[7] Latimer, A. A. *et al.* A theoretical study of methanol oxidation on RuO_2(110): bridging the pressure gap. *ACS Catal.* **7**, 4527–4534 (2017). **[Supplementary Information Page 82, Line 13–14]**

4. In Figure 1, the authors state that F–RuO_2 is positioned at the bottom of the volcano inversion diagram; however, the introduction of F only induces a slight symmetry breaking. Further validation is required to confirm whether this conclusion aligns with the simulation results for other halogens (e.g., Cl and Br), thereby avoiding overinterpretation of a single data point. Additionally, more detailed information should be provided to compare the local structural changes in RuO_2 after substitution by different elements (e.g., bond lengths, bond angles).

[**Author's Response**]: Thank you for your honest advice. We deeply agree with this view, so that the models of Cl–RuO_2 and Br–RuO_2 were constructed using Cl and Br as dopants, respectively. According to the DFT calculation analysis, compare to F–RuO_2, the incorporation of Cl or Br induces more pronounced symmetry–breaking in the octahedral configuration of RuO_2 (**Fig. 1f** and **Table S1**). **[Page 6, Line 7–8]**

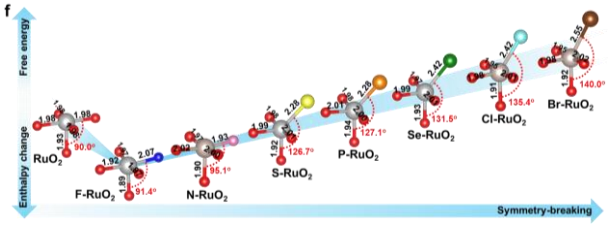

Figure 1. DFT calculations. (**f**) Reaction free energy (RDS) and subsurface O loss enthalpy change volcano against the symmetry–breaking.

Table S1. Bond angle of different catalysts.

Catalysts	Bond angle
F–RuO_2	91.4
RuO_2	90.0
N–RuO_2	95.1
S–RuO_2	126.7
P–RuO_2	127.1
Se–RuO_2	131.5
Cl–RuO_2	135.4
Br–RuO_2	140.0

5. In Figure 1, the authors do not address potential overlooked factors in the DFT simulations (e.g., solvent effects, zero–point energy corrections). It is recommended to include a critical evaluation of the model's assumptions, such as whether the effect of octahedral distortion on oxygen vacancy (O_V) formation energy has been overestimated.

[**Author's Response**]: Thank you for your professional comment. The Gibbs free energy change during OER was calculated by $\Delta G = \Delta E + \Delta ZPE - T\Delta S$, where the ΔE is the energy change of intermediates adsorbed on catalysts surface based on the DFT calculations, ΔZPE and ΔS is the change in zero–point energy and entropy, respectively, T is room temperature (298.15 K). According to your suggestion, we have included consideration of solvent effects in the model construction when recalculating the octahedral distortion on the O_V formation energy by including a Water Bi–layer water model to represent the interaction between the solvent water and the model surface (**Fig. 1e** and **Supplementary Fig. 23–30**). **[Page 5, Line 22–Page 6, Line 2]**

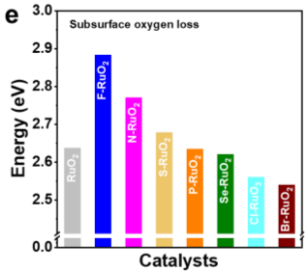

Figure 1. DFT calculations. (**e**) Calculated enthalpy changes for subsurface oxygen loss of various catalysts.

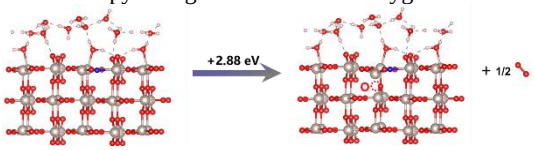

Supplementary Fig. 23. Atomistic structures showing the detachment of subsurface O from F–RuO_2(110) surface. The grey, red, blue and white balls represent Ru, O, F and H atoms, respectively.

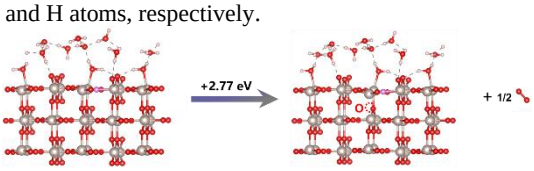

Supplementary Fig. 24. Atomistic structures showing the detachment of subsurface O from N–RuO_2(110) surface. The grey, red, pink and white balls represent Ru, O, N and H atoms, respectively.

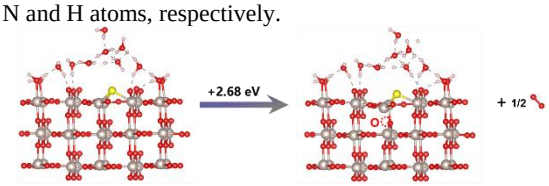

Supplementary Fig. 25. Atomistic structures showing the detachment of subsurface O from S–RuO_2(110) surface. The grey, red, yellow and white balls represent Ru, O, S and H atoms, respectively.

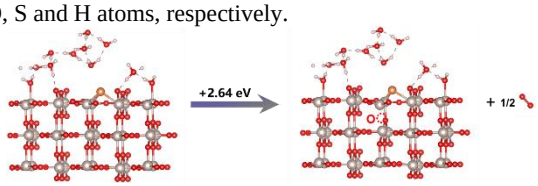

Supplementary Fig. 26. Atomistic structures showing the detachment of subsurface O from P–RuO_2(110) surface. The grey, red, orange and white balls represent Ru, O, P and H atoms, respectively.

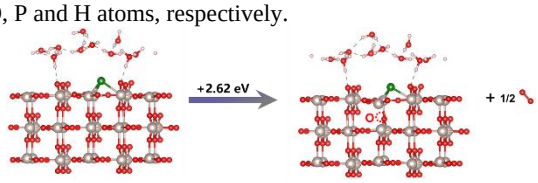

Supplementary Fig. 27. Atomistic structures showing the detachment of subsurface O from Se–RuO_2(110) surface. The grey, red, green and white balls represent Ru, O, Se and H atoms, respectively.

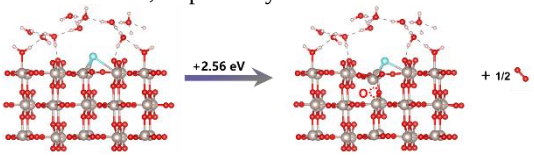

Supplementary Fig. 28. Atomistic structures showing the detachment of subsurface O from Cl–RuO_2(110) surface. The grey, red, cyan and white balls represent Ru, O, Cl and H atoms, respectively.

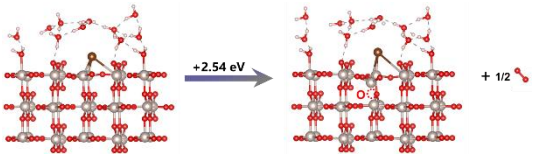

Supplementary Fig. 29. Atomistic structures showing the detachment of subsurface O from Br–RuO_2(110) surface. The grey, red, brown and white balls represent Ru, O, Br and H atoms, respectively.

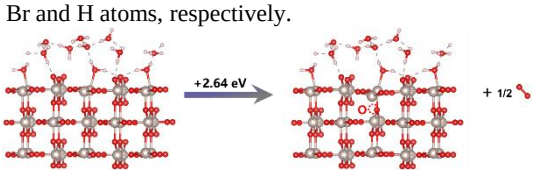

Supplementary Fig. 30. Atomistic structures showing the detachment of subsurface O from RuO_2(110) surface. The grey, red, and white balls represent Ru, O and H atoms, respectively.

6. In Figure 1, the authors briefly describe the mechanism by which F suppresses Ru dissolution (e.g., O–2p band center shift). It is suggested to integrate Bader charge analysis to elucidate how F enhances stability through electronic structure regulation and discuss its applicability under various acidic conditions.

[**Author's Response**]: Thank you for your valuable suggestions. In fact, charge density difference and Bader charge were presented in **Fig. 3g–j**. The valence state of Ru (+1.34) in F–RuO_2 decreases with increasing surrounding electron density, attributing to the electron density surrounding Ru was readjusted as a result of the octahedral symmetry breakdown induced by the highly electronegative F, potentially altering the adsorption of intermediates on RuO_2 and thereby switching the reaction route (**Fig. 3g–j**). **[Page 9, Line 4–8]**

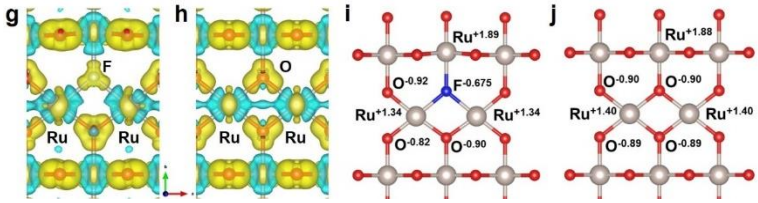

Figure 3. Electronic structure investigation. Electron density difference of (**g**) F–RuO_2/FC and (**h**) RuO_2. The blue and yellow shaded area mean the electron density accumulation and donation and the isosurface value is 0.065 e/Å^3. Bader charge analysis for Ru (grey), F (blue), and O (red) sites of (**i**) F–RuO_2/FC and (**j**) RuO_2.

Additionally, F–RuO_2/FC shows clearly pH–independence, suggesting the significant suppression of the LOM pathway and the dominant role of the AEM pathway (**Supplementary Fig. 71**).[47, 48] **[Page 12, Line 10–12]**

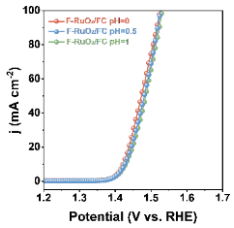

Supplementary Fig. 71. OER polarization curves of F–RuO_2/FC in various pH–H_2SO_4 electrolytes.

[47] Shi, Z. *et al.* Confined Ir single sites with triggered lattice oxygen redox: toward boosted and sustained water oxidation catalysis. *Joule* **5**, 2164–2176 (2021). **[Page 18, Line 7–8]**
[48] Wu, L. *et al.* Role of interfacial water in improving the activity and stability of lattice–oxygen–mediated acidic oxygen evolution on RuO_2. *Angew. Chem. Int. Ed.* e202420848 (2025). **[Page 18, Line 9–10]**

7. In Figures 2–3, the lattice strain mechanism induced by F is insufficiently explained. The interaction between the F–O bond and Ru–O bond should be clarified using DFT calculations.

[**Author's Response**]: Thanks for your carefully reading of our manuscript. We will systematically address your questions through the following two sections:

Part I: To address your concerns, we condected comprehensive characterization of the crystal structure of F–RuO_2/FC using advanced techniques including spherical aberration–corrected high–

angle annular dark–field scanning transmission electron microscopy (AC–HAADF–STEM), time of flight secondary ion mass spectrometry (TOF–SIMS) and X–ray diffraction (XRD) with Rietveld refinement. The result of analysis revealing that the partial substitution of O by F in RuO_2, inducing slight distortion in the octahedral configuration. The detailed analysis is presented below:

Firstly, to verify the lattice strain mechanism induced by F, long–range ordered atomic arrangements were successfully detected using a spherical AC–HAADF–STEM (**Fig. 2a**). The well–defined lattice spacings (0.22 and 0.18 nm) of (020) and $(21\bar{1})$ planes for RuO_2 unequivocally indicate the presence of lattice strain compared to RuO_2, which may be caused by symmetry breaking due to introduction of heterogeneous atoms (**Fig. 2b**). The fast Fourier transform (FFT) pattern, inset in **Fig. 2b**, reveals the exposed (020) and $(21\bar{1})$ planes along the $[\bar{1}0\bar{2}]$ zone axis of F–RuO_2/FC. To confirm the heterogeneous atoms in F–RuO_2/FC, STEM energy dispersive spectrometer (STEM–EDS) elemental mappings were conducted in **Fig. 2c**. In addition to the uniformly distributed Ru and O elements, conspicuous F signals can be observed, suggesting that the lattice strain in F–RuO_2/FC may be caused by the incorporation of F. **[Page 7, Line 1–11]**

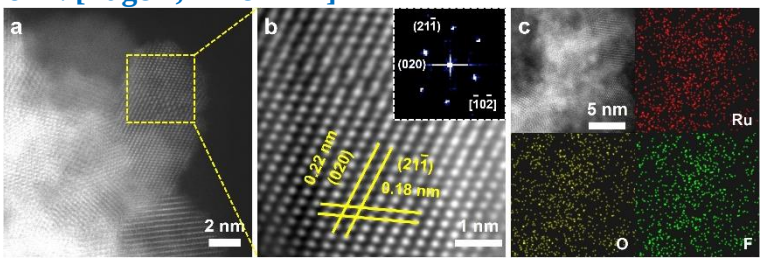

Figure 2. Structural characterizations. (**a**, **b**) spherical aberration–corrected HAADF–STEM images, (**c**) STEM–EDS elemental mappings of F–RuO_2/FC. Inset in (**b**) is the FFT pattern of F–RuO_2/FC.

Secondly, geometrical phase analysis (GPA) was performed to evaluate the strain level and distribution in the F–RuO_2/FC. Evidently, the reduced and enhanced strain can be observed along the horizontal (ε_{xx}) and vertical (ε_{yy}) direction, respectively (**Fig. 2d, e**). The strain profiles of line1 and line2 acquired from strain mappings further confirm that the compressive stress is predominantly along the ε_{xx} direction and the tension stress along the ε_{yy} direction (**Fig. 2f**).[37] **[Page 7, Line 11–15]**

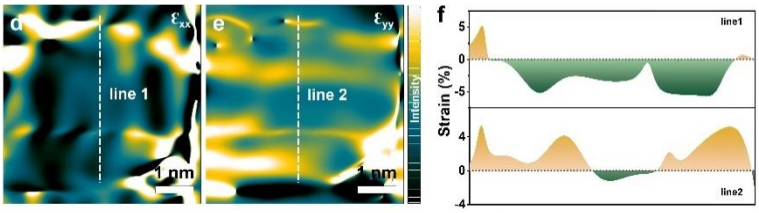

Figure 2. Structural characterizations. Strain mappings of F–RuO_2/FC along (**d**) ε_{xx} and (**e**) ε_{yy} direction from GPA and (**f**) line profiles of strain along the dotted white lines in (**d**) and (**e**).

Thirdly, to investigate the critical insight of chemical distributions for F–RuO_2/FC, TOF–SIMS analysis was performed in **Fig. 2g**. The element intensity versus sputter time reveals that the concentration of O^- is notably greater than that of Ru^+, being consistent with the characteristics of RuO_2. In addition, the detected RuF^- signals indicate that F indeed replaces part of O and then bonds with Ru during the heat treatment process. Two–dimensional (2D) TOF–SIMS elemental mappings also confirm the presence of significant RuF^- species alongside the abundant Ru and O species (**Fig. 2h**). Clearly, the distribution of Ru and O signals throughout the space in three–dimensional (3D) TOF–SIMS views indicates that the predominant species is RuO_2, consistent with the AC–HAADF–STEM analysis (**Fig. 2i**). The uniform distribution of RuF^- signals throughout the entire 3D space further confirms the partial substitution of O by F, thus leading to the formation of Ru–F bonds. **[Page 7, Line 15–Page 8, Line 2]**

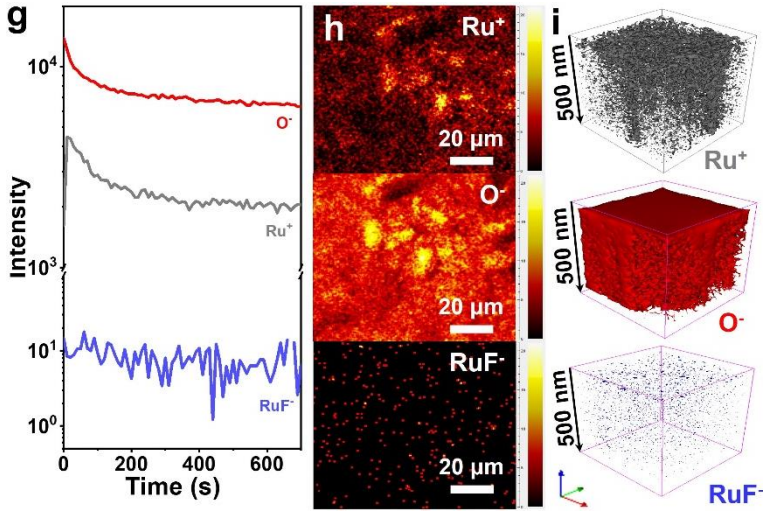

Figure 2. Structural characterizations. (**g**) TOF–SIMS depth analysis of Ru^+, O^-, and RuF^- for F–RuO_2/FC and (**h**) corresponding 2D elemental mapping images and (**i**) 3D render overlay images.

Finally, XRD with Rietveld refinement was conducted to obtain the detailed unit cell parameter (**Fig. 2j** and **Table S2**). The sharp diffraction peaks correspond to the tetragonal RuO_2 with the space group *P42/mnm*, indicating that the adsorbed $RuCl_3$ on the surface of FC gradually crystallizes into RuO_2 during the heat treatment process. The presence of Ru accelerates the local pyrolysis of FC and resulting in F occupying part of the position of O in F–RuO_2/FC (inset in **Fig. 2j**). **[Page 8, Line 2–7]**

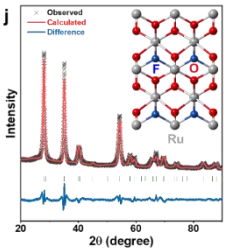

Figure 2. Structural characterizations. (**j**) XRD pattern of F–RuO_2/FC. Inset in (**j**) is structural model of F–RuO_2/FC.

Table S2. Refined parameters of F–RuO_2/FC.

F–RuO_2/FC	X	Y	Z
Ru0	0.500000	0.500000	0.500000
Ru1	0.000000	0.000000	0.000000
O2	0.694330	0.694330	0.000000
O3	0.194330	0.805670	0.500000
O4	0.239972	0.225644	–9.999990
F1	0.805670	0.194330	0.500000
a = 4.5436 Å, b = 4.5436 Å, c = 3.1397 Å, space grpup *P42/mnm*, R_{wp} = 6.12%, R_p = 4.70%, Chi2 = 8.977			

Part II: It is worth noting that the F–O bond mentioned by the reviewers is not covered in this manuscript. To avoid ambiguity, we clearly defined the descriptions of Ru–O or Ru–F bonds and clarified their interactions in our revised manuscript, and as follows:

The chemical structure and coordination environment of the F–RuO_2/FC was analyzed by Fourier transform of the EXAFS (FT–EXAFS) spectra, where the peak at ~1.42 Å in F–RuO_2/FC can be attributed to Ru–O or Ru–F coordination environment (denote as Ru–O/F) (**Fig. 3f** and **Supplementary Fig. 38**). **[Page 8, Line 22–Page 9, Line 2]**

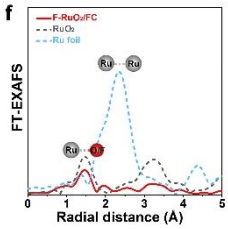

Figure 3. Electronic structure investigation. (**f**) EXAFS of F–RuO_2/FC, Ru foil and RuO_2.

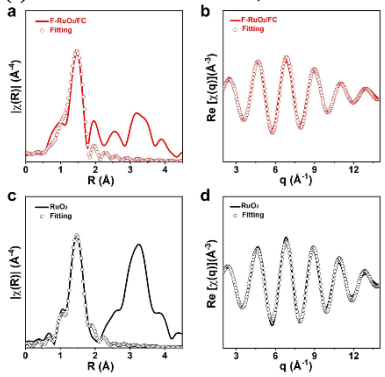

Supplementary Fig. 38. (**a**, **c**) R space and (**b**, **d**) inverse FT–EXAFS results of Ru K–edge for (**a**, **b**) F–RuO_2/FC and (**c**, **d**) RuO_2.

Compared to RuO_2, a noticeable red shift can be observed in the vibration peaks of F–RuO_2/FC, which may be caused by the shortened Ru–O owing to the partial substitution of O by the highly electronegative F (**Fig. 3a**).[39] Therefore, F 1s XPS spectra of F–RuO_2/FC present a wider peak than that of FC, corresponding to the C–F and Ru–F species (**Fig. 3b**). Additionally, O 1s XPS peaks of RuO_2 are located at 529.0, 530.0, and 531.7 eV, corresponding to O_L, O_V, and surface–adsorbed H_2O, respectively (**Fig. 3c**).[40, 41] Evidently, a notable shift of the O species towards higher binding energy can be observed in F–RuO_2/FC due to the presence of high electronegativity F results in an altered electronic interaction between Ru and O.[39] **[Page 8, Line 8–17]**

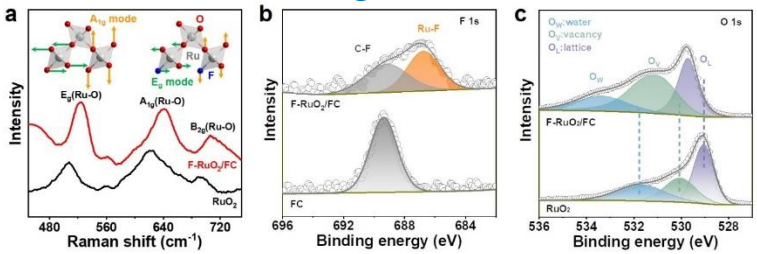

Figure 3. Electronic structure investigation. (**a**) Raman spectra of F–RuO_2/FC and RuO_2. (**b**) F 1s XPS spectra of F–RuO_2/FC and FC. (**c**) O 1s XPS spectra of F–RuO_2/FC and RuO_2.

In addition, the valence state of Ru (+1.34) in F–RuO_2 decreases with increasing surrounding electron density, attributing to the electron density surrounding Ru was readjusted as a result of the octahedral symmetry breakdown induced by the highly electronegative F, potentially altering the adsorption of intermediates on RuO_2 and thereby switching the reaction route (**Fig. 3g–j**). **[Page 9, Line 4–8]**

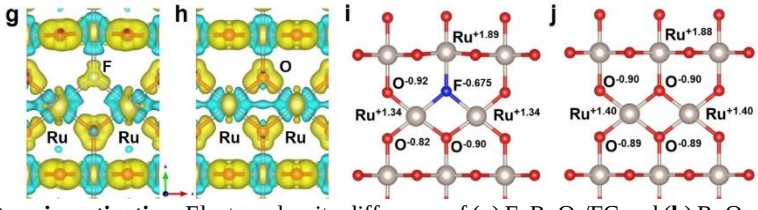

Figure 3. Electronic structure investigation. Electron density difference of (**g**) F–RuO_2/FC and (**h**) RuO_2. The blue and yellow shaded area mean the electron density accumulation and donation and the isosurface value is 0.065 e/Å^3. Bader charge analysis for Ru (grey), F (blue), and O (red) sites of (**i**) F–RuO_2/FC and (**j**) RuO_2.

[37] Wu, G. *et al.* In–plane strain engineering in ultrathin noble metal nanosheets boosts the intrinsic electrocatalytic hydrogen evolution activity. *Nat. Commun.* **13**, 4200 (2022). **[Page 17, Line 17–18]**
[39] Xiao, K., Wang, Y., Wu, P., Hou, L. & Liu, Z. Q. Activating lattice oxygen in spinel $ZnCo_2O_4$ through filling oxygen vacancies with fluorine for electrocatalytic oxygen evolution. *Angew. Chem. Int. Ed.* **62**, e202301408 (2023). **[Page 17, Line 21–23]**

[40] Liu, Z. *et al.* Optimal geometrical configuration of cobalt cations in spinel oxides to promote oxygen evolution reaction. *Angew. Chem. Int. Ed.* **59**, 4736–4742 (2020). **[Page 17, Line 24–25]**
[41] Xue, J. Y. *et al.* Engineering multiphasic $MoSe_2$/NiSe heterostructure interfaces for superior hydrogen production electrocatalysis. *Appl. Catal. B–Environ.* **312**, 121434 (2022). **[Page 17, Line 26–27]**

8. In Figure 3, the Ru valence states predicted by DFT (e.g., average oxidation state reduced to +3.5) should be quantitatively correlated with experimental data (e.g., XPS Ru 3p peak negative shift). The original paper only provides a qualitative description of "electron density adjustment." It is recommended to quantify the polarization effect of F on Ru charge using Bader charge analysis and compare it with relevant experimental characterization results (e.g., XPS and EXAFS).

[**Author's Response**]: Thank you for your guidance on our manuscript, which help to improve the quality of our work. According to your suggestiions, X–ray photoelectron spectroscopy (XPS) was performed on F–RuO_2/FC. Compared with RuO_2, Ru 3p XPS peaks for F–RuO_2/FC are negative shift of 0.35 eV, revealing a lower valence state than Ru^{4+} (**Fig. 3d**). Furthermore, X–ray absorption near–edge structure (XANES) showed a lower absorption energy for F–RuO_2/FC compared to RuO_2 suggests that the average valence state of Ru in F–RuO_2/FC is below +4, which is attributed to the partial substitution of O by highly electronegative F (**Fig. 3e**). In addition, charge density difference and Bader charge analysis also reveals that the valence state of Ru (+1.34) in F–RuO_2 decreases with increasing surrounding electron density, which is consistent with the results from XPS and XANES analyses (**Fig. 3g–j**). **[Page 8, Line 17–22 and Page 9, Line 4–8]**

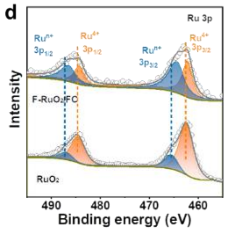

Figure 3. Electronic structure investigation. (**d**) Ru 3p XPS spectra of F–RuO_2/FC and RuO_2.

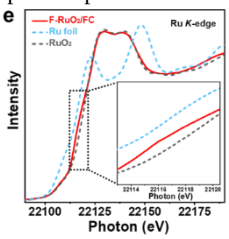

Figure 3. Electronic structure investigation. Ru K–edge (**e**) XANES of F–RuO_2/FC Ru foil and RuO_2.

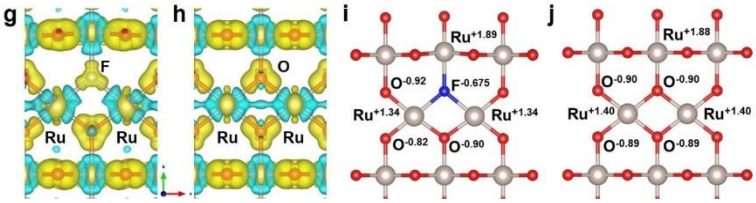

Figure 3. Electronic structure investigation. Electron density difference of (**g**) F–RuO_2/FC and (**h**) RuO_2. The blue and yellow shaded area mean the electron density accumulation and donation and the isosurface value is 0.065 e/Å^3. Bader charge analysis for Ru (grey), F (blue), and O (red) sites of (**i**) F–RuO_2/FC and (**j**) RuO_2.

9. In Figure 4, the authors do not explicitly clarify whether resistance voltage drop (iR) correction has been applied to the overpotential (η). In acidic electrolytes, electrode interface impedance (R_total) may lead to an overestimation of η, particularly when the catalyst exhibits poor conductivity (e.g., RuO_2–based materials).

[**Author's Response**]: Thank you for your scrutiny of our manuscript. According to your consideration, we define the detail electrochemical measurements process in methods section, in which 95% iR compensation have been implemented on the LSV polarization curves.

Electrochemical measurements. All polarization curves (95% iR compensation) are averages of the multiple test results at 5 mV s^{-1}. **[Page 14, Line 18–19]**

10. In Figure 4, the author merely claims that "F introduces more active sites," which lacks robust and direct evidence.

[**Author's Response**]: Thanks for your perceptive observations regarding this study. To strengthen this conclusion, this intrinsic activity of individual Ru sites was evaluated through the calculations of turnover frequency (TOF) (**Supplementary Fig. 40**). Notable, the F–RuO_2/FC displays high intrinsic activity compare to RuO_2/C and RuO_2, demonstrating that F as a dopant effectively introduces more active sites. **[Page 9, Line 21–22]**

Calculation of the turnover frequency (TOF). At first, each Ru atom on the electrode was considered as an active site in the calculation process. The TOF of F–RuO_2/FC, RuO_2/C and RuO_2 were calculated according to equation (1).

$$\mathrm{TOF} = \frac{\text{Number of } O_2 \text{ per second}}{\text{Number of active Ru sites}} \quad (1)$$

The number of oxygen per second was obtained from the LSV curves according to equation (2).

$$\text{Number of } O_2 \text{ per second} = (|J|A)\left(\frac{1\ \mathrm{C}}{\mathrm{s}}\right)\left(\frac{1\ \mathrm{mol}}{96453.8\ \mathrm{C}}\right)\left(\frac{1\ \mathrm{mol}}{4\mathrm{e}}\right)\left(\frac{6.023\times10^{23}}{1\ \mathrm{mol}\ O_2}\right) \quad (2)$$

in which J is the geometric current.

The number of active Ru sites can be calculated following equation (3).

$$\text{Number of active Ru sites} = \frac{m_{cat}\times \text{Ru wt\%}}{101.07\ \mathrm{g\ mol^{-1}}} \times 6.023 \times 10^{23} \quad (3)$$

Where m_{cat} is the mass of catalysts loaded on the work electrode. **[Supplementary Information Page 2, Line 8–17]**

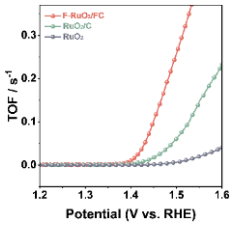

Supplementary Fig. 40. TOF of F–RuO_2/FC, RuO_2/C, and RuO_2.

11. The comparison between DFT predictions and experimental results remains superficial (e.g., only "symmetry breaking" is mentioned), and the adsorption energy or reaction pathway of key intermediates has not been quantitatively validated. It is recommended to include in the supplementary material a correlation between the ΔG* (OER steps) calculated via DFT and the Tafel slope measured experimentally to establish a clear theory–experiment mapping.

[**Author's Response**]: Thank you very much for the insightful and constructive comments, which have inspired us to futher refine our research work. As your suggestion, the Tafel slope of electrocatalysts were calculated base on LSV, which displaying a positive correlation with the Gibbs free energy of rate–determining step (RDS) (**Supplementary Fig. 65**).

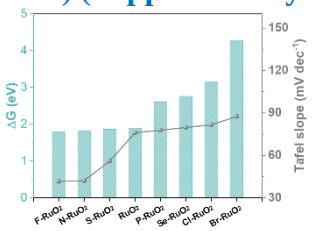

Supplementary Fig. 65. Gibbs free energy of RDS versus Tafel slope.

12. In Figure 5, no explicit correlation mechanism linking F doping with the AEM path has been established, and there is a lack of DFT transition state analysis or EXAFS surface coordination verification.

[**Author's Response**]: We sincerely appreciate your valuable feedback, which has helped us improve the manuscript. As shown in **Fig. 5f**, the LOM pathway that O_L is involved in the OER process, including a labeled ^{18}O and an ambient O (^{16}O) from the electrolyte, resulting in the instability surface of the RuO_2 and consequently generating $^{16}O^{18}O$ specie. Based on the DFT computations and detailed experimental characterization, the F induced symmetry–breaking in octahedral configuration of RuO_2 improves the interaction between adsorbent and the electrocatalysts surface, alters the OER route to follow the AEM pathway, and ultimately enhancing the electrocatalytic performance. **[Page 12, Line 21–Page 13, Line 4]**

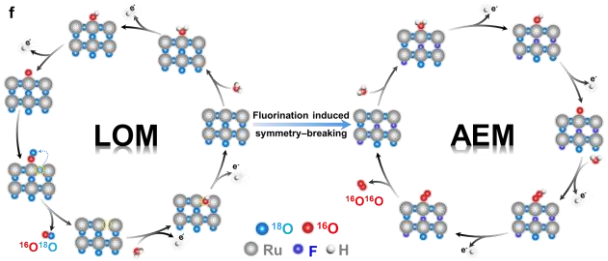

Figure 5. Mechanism explorations. (**f**) Schematic illustration of the mechanism transformation from LOM to AEM caused by F–mediated symmetry breaking on RuO_2.

The chemical structure and coordination environment of the F–RuO_2/FC was analyzed by Fourier transform of the EXAFS (FT–EXAFS) spectra, where the peak at ~1.42 Å in F–RuO_2/FC can be attributed to Ru–O or Ru–F coordination environment (denote as Ru–O/F) (**Fig. 3f** and **Supplementary Fig. 38**). Obviously, the diminished intensity of Ru–O/F bonds for F–RuO_2/FC as opposed to RuO_2 suggests that the introduction of F leads to an unsaturated coordination environment (**Table S3**). **[Page 8, Line 22–Page 9, Line 4]**

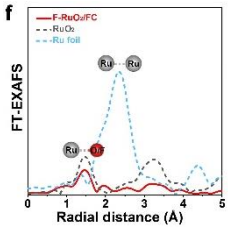

Figure 3. Electronic structure investigation. (**f**) EXAFS of F–RuO_2/FC, Ru foil and RuO_2.

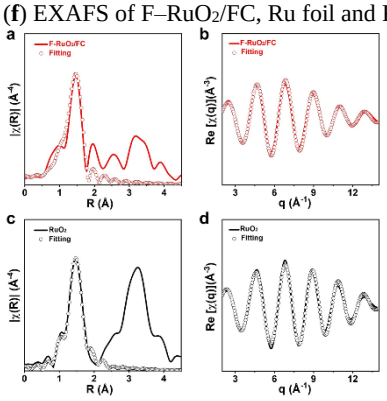

Supplementary Fig. 38. (**a**, **c**) R space and (**b, d**) inverse FT–EXAFS results of Ru K–edge for (**a**, **b**) F–RuO_2/FC and (**c, d**) RuO_2.

Table S3. Structural parameters obtained from the curve–fitting analysis of the Ru K–edge EXAFS spectra.

Sample	Shell	*N*	*R*(Å)	σ^2(10^{-3} Å^2)	*R* factor
F–RuO_2/FC	Ru–O(F)	5.7	1.95	5.85	0.017
RuO_2	Ru–O	6.0	1.96	2.44	0.015

Note:
N is the coordination number.
R is interatomic distance (the bond length between central atoms and surrounding coordination atoms).
σ^2 is Debye–Waller factor (a measure of thermal and static disorder in absorber–scatterer distances).
R factor is residual factor.

13. Inferring from XRD structural stability that O does not participate in the reaction involves a logical leap; oxygen isotope tracking data should be incorporated for validation.

[**Author's Response**]: Thank you for your professional suggestions. In the original manuscript, we have already conducted O–isotope tracking experiments, which are described as follows:

Operando differential electrochemical mass spectrometry (DEMS) was performed on ^{18}O isotope–labelled F–RuO_2/FC using linear sweep voltammograms (LSV) in $H_2{}^{16}O$ 0.5 M H_2SO_4 (**Supplementary Fig. 73a**). As shown in **Fig. 5e**, the mass signals of $^{32}O_2$ and $^{34}O_2$ were detected without $^{36}O_2$ products, suggesting the non–participation of O_L in the OER process. The mass signals of $^{32}O_2$ gradually increase and present a constant ratio ($^{32}O_2$:$^{34}O_2$) with the occurrence of OER, further demonstrating the dominant AEM pathway (**Supplementary Fig. 73b, c**). **[Page 12, Line 16–21]**

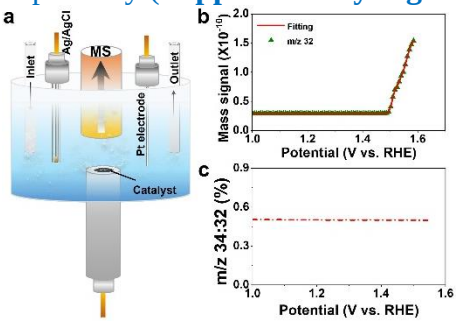

Supplementary Fig. 73. (**a**) Schematic illustration of the operando DEMS device. (**b**) DEMS signals of $^{32}O_2$ (^{16}O + ^{16}O) were collected during the LSV cycle. (**c**) Ratio of $^{34}O_2$:$^{32}O_2$ within the LSV range.

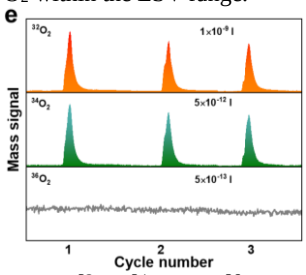

Figure 5. Mechanism explorations. (**e**) DEMS signals of $^{32}O_2$, $^{34}O_2$, and $^{36}O_2$ from the gaseous products for ^{18}O–labeled F–RuO_2/FC catalysts in $H_2{}^{16}O$ aqueous H_2SO_4 electrolyte during three times of LSV cycles.

14. It is suggested that the conclusion propose additional research directions, such as investigating the impact of other halogens (Cl, Br) or non–elemental doping on symmetry breaking and OER properties, as well as exploring the potential characteristics and performance of the catalyst under reaction conditions.

[**Author's Response**]: Thanks for your kind suggestion. Based on your consideration, the models of Cl–RuO_2 and Br–RuO_2 were constructed using Cl and Br as dopants, respectively. According to the DFT calculation analysis, compare to F–RuO_2, the incorporation of Cl or Br leads to a higher reaction energy barrier and a lower formation energy of O_V for RuO_2, indicating that excessive symmetry breaking also affects the activity and stability of RuO_2 (**Fig. 1c, e,** and **f**). **[Page 4, Line 19–21 and Page 5, Line 23–Page 6, Line 2]**

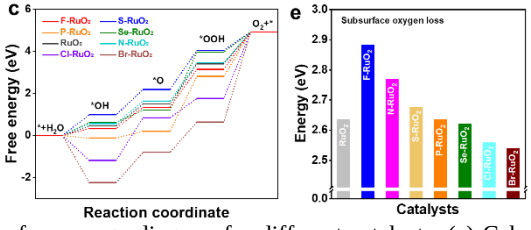

Figure 1. DFT calculations. (**c**) Gibbs free energy diagram for different catalysts. (**e**) Calculated enthalpy changes for subsurface oxygen loss of various catalysts.

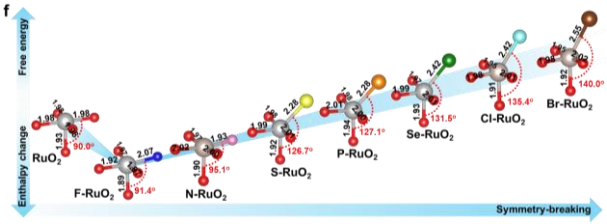

Figure 1. DFT calculations. (**f**) Reaction free energy (RDS) and subsurface O loss enthalpy change volcano against the symmetry–breaking.

Subsequently, Cl–RuO_2/(F)C and Br–RuO_2/(F)C were synthesized in **Supplementary Fig. 62, 63.**

Preparation of RuO_2/(F)C. The synthesis condition of RuO_2/(F)C is the same as F–RuO_2/FC, except that the FC used for RuO_2/(F)C was pre–annealed in air at 400 °C for 12 h to remove F (denoted as (F)C). **[Page 14, Line 3–4]**

Preparation of M–RuO_2/(F)C (M = N, S, P, Se, Cl and Br). The M–RuO_2/(F)C electrocatalyst was synthesized by vapor transport method, where the anion–donating powder and RuO_2/(F)C (mass ratio 1:2) were placed at the upstream and downstream positions of a quartz tube, respectively. The anion–donating powder and RuO_2/(F)C were heated to the target temperature and 400 °C respectively at a heating rate of 5 °C min^{-1} in an Ar atmosphere and maintained for 1 h to obtain M–RuO_2/(F)C. In addition, melamine, sulfur powder, sodium hypophosphite, selenium powder, a mixture of polyvinyl chlorid and manganese dioxide, and hexabromobenzene were unsed as anion sources, releasing anions under heat treatment at 450 °C, 150 °C, 300 °C, 500 °C, 450 °C, and 350 °C, respectively. **[Page 14, Line 5–12]**

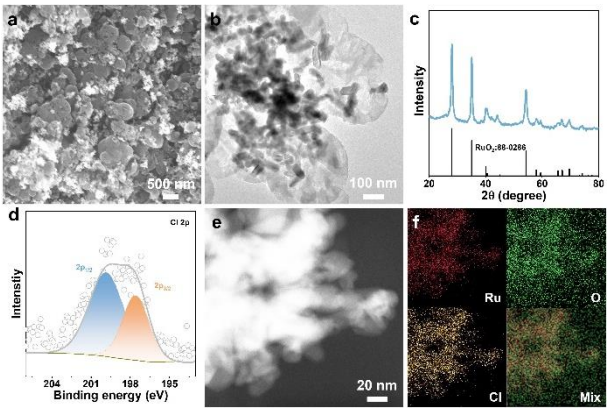

Supplementary Fig. 62. (**a**) SEM image, (**b**) TEM image, (**c**) XRD pattern, (**d**) Cl 2p XPS spectrum, (**e**) STEM image, and (**f**) STEM–EDS elemental mappings of Cl–RuO_2/(F)C.

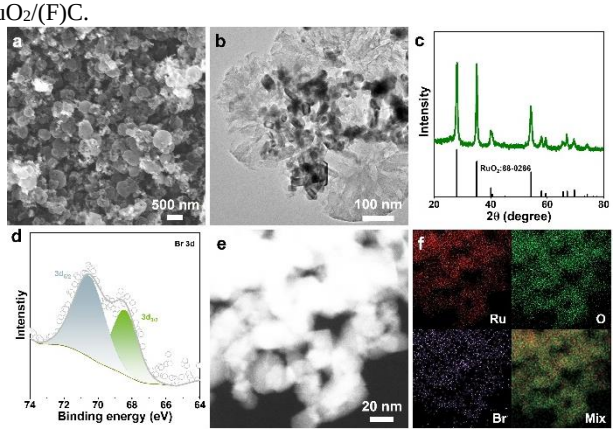

Supplementary Fig. 63. (**a**) SEM image, (**b**) TEM image, (**c**) XRD pattern, (**d**) Br 3d XPS spectrum, (**e**) STEM image, and (**f**) TEM–EDS elemental mappings of Br–RuO_2/(F)C.

The activity and stability of Cl–RuO_2/(F)C and Br–RuO_2/(F)C showed markedly reduced compared to F–RuO_2/FC, which is consistent with the results predicted by DFT calculations (**Supplementary Fig. 64**). **[Page 10, Line 16–19]**

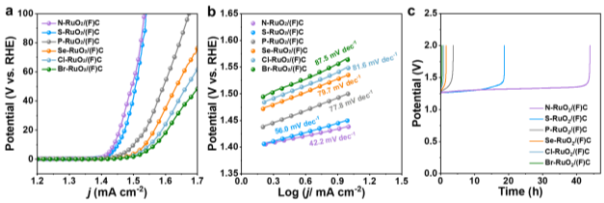

Supplementary Fig. 64. (**a**) OER polarization curves, (**b**) Tafel plots, and (**c**) chronopotentiometry tests of N–RuO_2/(F)C, S–RuO_2/(F)C, P–RuO_2/(F)C, Se–RuO_2/(F)C, Cl–RuO_2/(F)C and Br–RuO_2/(F)C.

15. The description of the DFT calculation method omits several critical details, including the model size, whether atoms are fixed, how the adsorption site is determined, and how free energy is calculated and corrected. It is recommended that the authors consult relevant literature to provide a comprehensive description to ensure the reproducibility of the computational results.

[**Author's Response**]: We sincerely appreciate your valuable suggestions. The comprehensive DFT calculation details were added to the methods section in our revised manuscript.

DFT calculations were conducted using the Vienna ab initio simulation package (VASP), which employed the projector augmented wave (PAW) method to simulate the electron–ions interactions.[1, 2] The exchange–correction interactions were described by the generalized gradient approximation (GGA) of the Perdew–Burke–Ernzerhof (GGA–PBE).[3] The RuO_2(110) facet was selected because it exposes fully coordinated bridged Ru sites and coordination unsaturated sites with quintuple coordination that bind to triple–coordinated O for better identification of the active site.[4–6] Additionally, this surface is known to exhibit the most favorable thermodynamic free energy during most synthesis processes, as established in prior studies.[7] The cutoff energy was set as 400 eV during the structural optimization of all slab models. During the structural optimization calculations, the atoms in the bottom two layers were fixed and other layers of atoms were allowed to relax. The vacuum layer above the surface is at least 15 Å, and the calculation module was placed in a 6.2146 Å × 12.6698 Å × 21.7973 Å lattice. The k–points (Monkhorst–Pack mesh) during the structural optimization and electronic structure–involved calculations were set to 4 × 2 × 1 and 5 × 5 × 1, respectively.

The Gibbs free energy change during OER was calculated by $\Delta G = \Delta E + \Delta ZPE - T\Delta S$, where the ΔE is the energy change of intermediates adsorbed on catalysts surface based on the DFT calculations, ΔZPE and ΔS is the change in zero-point energy and entropy, respectively, T is room temperature (298.15 K). The free energy of $(H^+ + e^-)$ at standard conditions was assumed as the energy of 1/2 H_2. Namely, $G(H^+ + e^-) = 1/2G(H_2)$. $G(OH^-) = G(H_2O) - 1/2G(H_2)$. **[Supplementary Information Page 3, Line 8–25]**

[1] Kresse, G. & Furthmüller, J. Efficiency of ab–initio total energy calculations for metals and semiconductors using a plane–wave basis set. *Comput. Mater. Sci.* **6**, 15–50 (1996). **[Supplementary Information Page 82, Line 2–3]**

[2] Blöchl, P. E. Projector augmented–wave method. *Phys. Rev. B* **50**, 17953–17979 (1994). **[Supplementary Information Page 82, Line 4]**

[3] Perdew, J. P., Burke, K. & Ernzerhof, M. Generalized gradient approximation made simple. *Phys. Rev. Lett.* **77**, 3865–3868 (1996). **[Supplementary Information Page 82, Line 5–6]**

[4] Sun, Q. *et al.* Effect of a humid environment on the surface structure of RuO_2(110). *Phys. Rev. B* **67**, 205424 (2003). **[Supplementary Information Page 82, Line 7–8]**

[5] Abbott, D. F. *et al.* Oxygen reduction on nanocrystalline ruthenia–local structure effects. *RSC Adv.* **5**, 1235–1243 (2014). **[Supplementary Information Page 82, Line 9–10]**

[6] Rao, R.R. *et al.* Operando identification of site-dependent water oxidation activity on ruthenium dioxide single–crystal surfaces. *Nat. Catal.* **3**, 516–525 (2020). **[Supplementary Information Page 82, Line 11–12]**

[7] Latimer. A A, *et al.* A theoretical study of methanol oxidation on RuO_2(110): bridging the pressure gap. *ACS Catal.* **7**, 4527–4534 (2017). **[Supplementary Information Page 82, Line 13–14]**

In the end, we would like to thank for the precious time of the reviewers and the editor. We sincerely wish that our point-to-point response and the revised manuscript have addressed your concerns and

satisfy your requirements for publications. We would be grateful if we have the chance to share our work with readers of ***Nature Communications***.

Xiaoqing Huang

Response to Reviewers

To Reviewer 1:

General comment: The author provided some new materials in response to my questions, but most of my doubts remain unresolved.

[Author's Response]: We appreciate your precious time for reviewing our revised manuscript. During the revision process, we have indeed addressed all your concerns in detail. As you requested, we have carried out the following experiments to address your comments point-to-point.

1. Comment: First, the concept of symmetry breaking lacks a clear definition, along with quantitative metrics to measure its extent. The authors define symmetry breaking as "the structural modifications at atomic scale that reduce its crystal symmetry". However, this definition remains somewhat generalized and does not provide a clear method for quantifying the degree of symmetry breaking based on experimental evidence. Generally, any elemental doping or substitution will introduce atomic-scale structural modifications, which inherently trigger symmetry breaking.

[Author's Response]: Thanks for your perceptive observations and constructive feedback on this study. According to the literature (*Proc. Natl. Acad. Sci.* **93**, 14256–14259 (1996); *Science* **177**, 393-396 (1972)), symmetry breaking is a fundamental concept in physics, referring to the phenomenon where a system with originally high symmetry undergoes a reduction in its degree of symmetry due to the emergence of asymmetric factors. Considering Wang et al.'s (*Appl. Catal. B–Environ.* **316**, 121664 (2022)) recent application of the symmetry–breaking effect to materials chemistry and their clear definition, that is, defects in a crystal lattice lower the lattice's symmetry, which is known as the symmetry–breaking effect, we have thoroughly revised our manuscript.

Moreover, the Baur distortion index (D_i), proposed by Li et al. (*Nature* **620**, 328–335 (2023)), is used to quantify the asymmetry or distortion in the virtual octahedral units of crystal structures. Therefore, the Baur distortion index (D_i) was employed to quantify the degree of symmetry breaking of virtual octahedral units within the RuO_2 crystal structure:

$$D_i = \frac{1}{6}\sum_{i=1}^{6}\left(\frac{|b_i-\bar{b}|}{\bar{b}}\right)$$

where b_i and $\bar{b}$ represent the individual bond length and the average of six bond lengths, respectively.[41] Based on the Rietveld refinement of XRD patterns results (**Fig. 2j** and **Supplementary Fig. 40c, 41c, 42c, 43c, 44c and 45c**), the octahedral structural units of F–RuO_2/FC, N–RuO_2(F)C, S–RuO_2(F)C, P–RuO_2(F)C, Se–RuO_2(F)C, Cl–RuO_2(F)C and Br–RuO_2(F)C are depicted in **Supplementary Fig. 46 and Table S2–S8**. The calculated D_i were increase in the order F < N < S < P < Se < Cl < Br, indicating an increase of octahedral distortion degree, consistent with DFT predictions. **[Page 8, Line 8–16]**

We agree with the reviewer's point that any elemental doping or substitution will introduce atomic–scale structural modifications, which inherently trigger symmetry breaking. Recently, Dai et al. also reviewed current symmetry–breaking methods (*Chem. Soc. Rev.* **54**, 3848–3905 (2025)), including doping—introducing heteroatoms (such as non–metals or metallic heteroatoms) and surface modification and defect engineering—introducing defect sites (e.g.,vacancies and lattice distortions) or modifying surfaces with specific functional groups. Therefore, in this study, the introduction of heteroatoms F, N, S, P, Se, Cl, and Br as asymmetric elements into the RuO_2 crystal structure can be categorized as a non–metal doping strategy to achieve symmetry breaking.

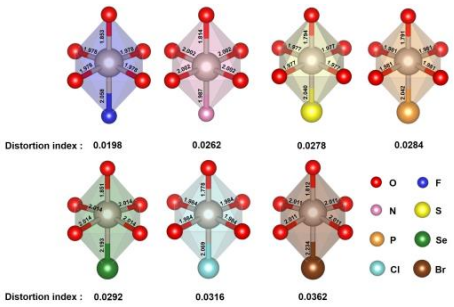

Supplementary Fig. 46. The metal–nonmetal bond length of F–RuO_2, N–RuO_2, S–RuO_2, P–RuO_2, Se–RuO_2, Cl–RuO_2 and Br–RuO_2 crystal structure. The calculated distortion indexes are indicated.

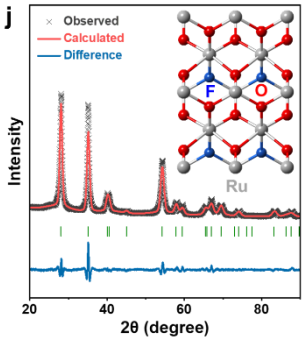

Figure 2. Structural characterizations. (**j**) XRD pattern of F–RuO_2/FC. Inset in (**j**) are the structural model of F–RuO_2/FC.

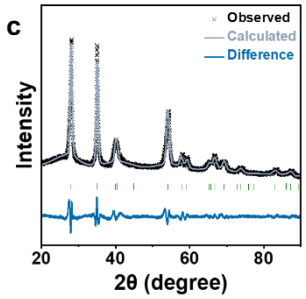

Supplementary Fig. 40. (**c**) XRD pattern of N–RuO_2/(F)C.

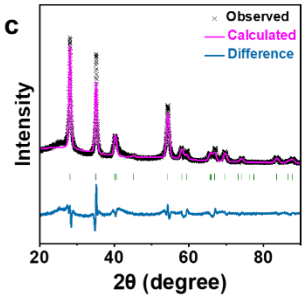

Supplementary Fig. 41. (**c**) XRD pattern of S–RuO_2/(F)C.

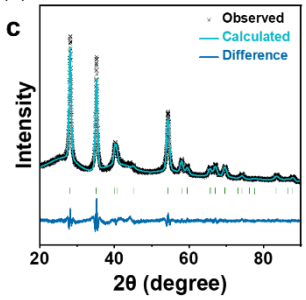

Supplementary Fig. 42. (**c**) XRD pattern of P–RuO_2/(F)C.

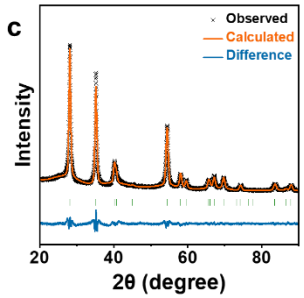

Supplementary Fig. 43. (**c**) XRD pattern of Se–RuO_2/(F)C.

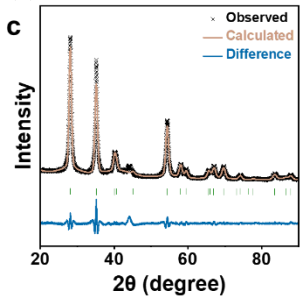

Supplementary Fig. 44. (**c**) XRD pattern of Cl–RuO_2/(F)C.

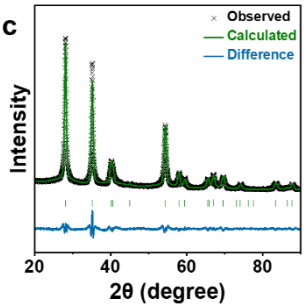

Supplementary Fig. 45. (**c**) XRD pattern of Br–RuO_2/(F)C.

Table S2. Refined parameters of F–RuO_2/FC.

F–RuO_2/FC	X	Y	Z
Ru0	0.48485	0.51515	0.50000
Ru1	0.01756	-0.01756	-0.00000
O2	0.69389	0.69616	0.00000
O3	0.19451	0.80549	0.50000
O4	0.30384	0.30611	-0.00000
F1	0.80534	0.19466	0.50000
a = 4.50909 Å, b = 4.50909 Å, c = 3.11133 Å, space grpup *P42/mnm*, R_{wp} = 5.59%, Chi2 = 7.53			

Table S3. Refined parameters of N–RuO_2/(F)C.

N–RuO_2/(F)C	X	Y	Z
Ru0	0.50883	0.49117	0.50000
Ru1	-0.01173	0.01173	-0.00000
O2	0.69264	0.69243	0.00000
O3	0.19586	0.80414	0.50000
O4	0.30757	0.30736	-0.00000
N1	0.80683	0.19317	0.50000
a = 4.52037 Å, b = 4.52037 Å, c = 3.12181 Å, space grpup *P42/mnm*, R_{wp} = 5.05%, Chi2 = 6.58			

Table S4. Refined parameters of S–RuO_2/(F)C.

S–RuO_2/(F)C	X	Y	Z
Ru0	0.48556	0.51444	0.50000
Ru1	0.01766	-0.01766	-0.00000
O2	0.68746	0.69669	0.00000
O3	0.20040	0.79960	0.50000
O4	0.30330	0.31254	-0.00000
S1	0.80561	0.19439	0.50000
a = 4.48394 Å, b = 4.48394 Å, c = 3.11028 Å, space grpup *P42/mnm*, R_{wp} = 6.44%, Chi2 = 8.25			

Table S5. Refined parameters of P–RuO_2/(F)C.

P–RuO_2/(F)C	X	Y	Z
Ru0	0.48025	0.51975	0.50000
Ru1	0.02406	-0.02406	-0.00000
O2	0.68849	0.69716	0.00000
O3	0.19748	0.80252	0.50000
O4	0.30284	0.31151	-0.00000
P1	0.80241	0.19759	0.50000
a = 4.50192 Å, b = 4.50192 Å, c = 3.10770 Å, space grpup *P42/mnm*, R_{wp} = 4.53%, Chi2 = 3.74			

Table S6. Refined parameters of Se–RuO_2/(F)C.

Se–RuO_2/(F)C	X	Y	Z
Ru0	0.47722	0.52278	0.50000
Ru1	0.03359	-0.03359	0.00000
O2	0.68462	0.69946	-0.00000
O3	0.19975	0.80025	0.50000
O4	0.30055	0.31538	0.00000
Se1	0.80428	0.19572	0.50000
a = 4.49913 Å, b = 4.49913 Å, c = 3.10685 Å, space grpup *P42/mnm*, R_{wp} = 4.46%, Chi2 = 3.72			

Table S7. Refined parameters of Cl–RuO_2/(F)C.

Cl–RuO_2/(F)C	X	Y	Z
Ru0	0.47924	0.52077	0.50000
Ru1	0.02721	-0.02721	-0.00000
O2	0.68822	0.69910	0.00000
O3	0.19879	0.80120	0.50000
O4	0.30090	0.31178	-0.00000
Cl1	0.80563	0.19437	0.50000
a = 4.49933 Å, b = 4.49933 Å, c = 3.10890 Å, space grpup *P42/mnm*, R_{wp} = 6.20%, Chi2 = 6.45			

Table S8. Refined parameters of Br–RuO_2/(F)C.

Br–RuO_2/(F)C	X	Y	Z
Ru0	0.47220	0.52780	0.50000
Ru1	0.03881	-0.03881	-0.00000
O2	0.68573	0.70042	0.00000
O3	0.19902	0.80098	0.50000
O4	0.29958	0.31427	-0.00000
Br1	0.80468	0.19532	0.50000
a = 4.50267 Å, b = 4.50267 Å, c = 3.10783 Å, space grpup *P42/mnm*, R_{wp} = 4.78%, Chi2 = 3.56			

[41] Najarian, A. M. *et al.* Homomeric chains of intermolecular bonds scaffold octahedral germanium perovskites. *Nature* **620**, 328–335 (2023). **[Page 18, Line 11–12]**

2. Comment: Current experimental evidence confirms the successful doping of elements, such as N, S, P, Se, Cl and Br into RuO_2. However, there is no definitive experimental data demonstrating how these dopants specifically change the degree of symmetry breaking.

[Author's Response] Thanks for your exceptional insights that fundamentally improved our work. Due to the combined influence of electronegativity, atomic radius, and so on, the introduction of different

heteroatoms causes changes in structural parameters like bond length, thus breaking the symmetry of the original structure. Thus, XRD Rietveld refinement was conducted to obtain the octahedral structure units of F–RuO_2/FC, N–RuO_2(F)C, S–RuO_2(F)C, P–RuO_2(F)C, Se–RuO_2(F)C, Cl–RuO_2(F)C, and Br–RuO_2(F)C (**Supplementary Fig. 40c, 41c, 42c, 43c, 44c and 45c, 46 and Table S2–S8**). Subsequently, the Baur distortion index (D_i) was employed to quantify the symmetry breaking degree of virtual octahedral units within the RuO_2 crystal structure:

$$D_i = \frac{1}{6}\sum_{i=1}^{6}\left(\frac{|b_i-\bar{b}|}{\bar{b}}\right)$$

where b_i and $\bar{b}$ represent the individual bond length and the average of six bond lengths, respectively.[41] **[Page 8, Line 8–13]**

As evidenced by the computational results based on the Rietveld refinement of XRD patterns results, a positive correlation exists between the D_i and octahedral distortion severity, with elevated D_i values directly correspond to both increased structural distortion and enhanced octahedral symmetry breaking. Therefore, incorporation of F, N, S, P, Se, Cl and Br elements into RuO_2 enables controlled symmetry breaking through modulation of the bond length in the octahedral coordination environment.

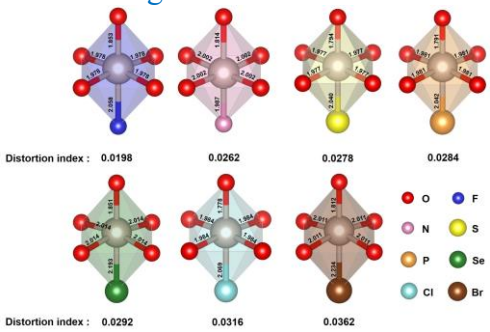

Supplementary Fig. 46. The metal–nonmetal bond length of F–RuO_2, N–RuO_2, S–RuO_2, P–RuO_2, Se–RuO_2, Cl–RuO_2 and Br–RuO_2 crystal structure. The calculated distortion indexes are indicated.

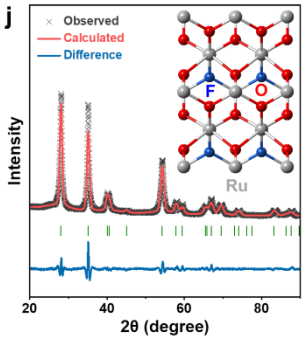

Figure 2. Structural characterizations. (**j**) XRD pattern of F–RuO_2/FC. Inset in (**j**) are the structural model of F–RuO_2/FC.

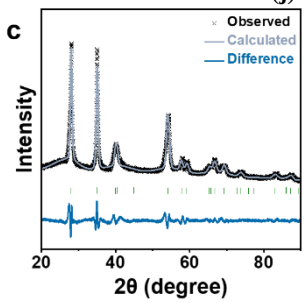

Supplementary Fig. 40. (**c**) XRD pattern of N–RuO_2/(F)C.

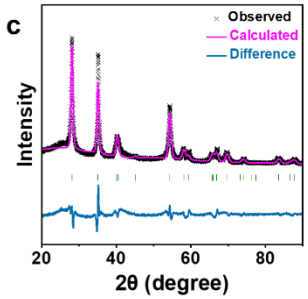

Supplementary Fig. 41. (**c**) XRD pattern of S–RuO_2/(F)C.

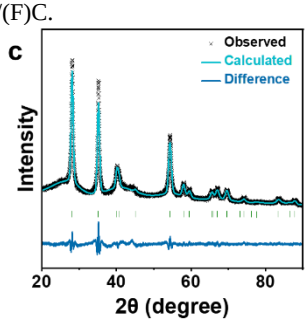

Supplementary Fig. 42. (**c**) XRD pattern of P–RuO_2/(F)C.

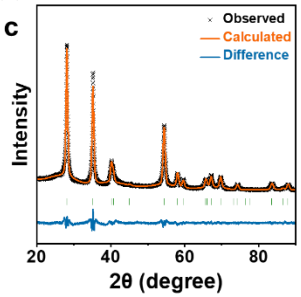

Supplementary Fig. 43. (**c**) XRD pattern of Se–RuO_2/(F)C.

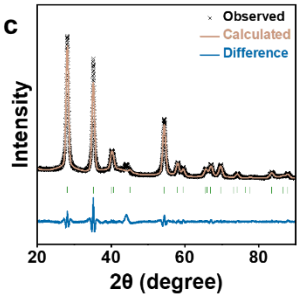

Supplementary Fig. 44. (**c**) XRD pattern of Cl–RuO_2/(F)C.

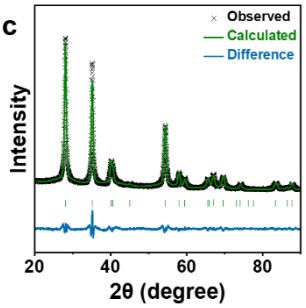

Supplementary Fig. 45. (**c**) XRD pattern of Br–RuO_2/(F)C.

Table S2. Refined parameters of F–RuO_2/FC.

F–RuO_2/FC	X	Y	Z
Ru0	0.48485	0.51515	0.50000
Ru1	0.01756	-0.01756	-0.00000
O2	0.69389	0.69616	0.00000
O3	0.19451	0.80549	0.50000
O4	0.30384	0.30611	-0.00000
F1	0.80534	0.19466	0.50000
a = 4.50909 Å, b = 4.50909 Å, c = 3.11133 Å, space grpup *P42/mnm*, R_{wp} = 5.59%, Chi2 = 7.53			

Table S3. Refined parameters of N–RuO_2/(F)C.

N–RuO_2/(F)C	X	Y	Z
Ru0	0.50883	0.49117	0.50000
Ru1	-0.01173	0.01173	-0.00000
O2	0.69264	0.69243	0.00000
O3	0.19586	0.80414	0.50000
O4	0.30757	0.30736	-0.00000
N1	0.80683	0.19317	0.50000
a = 4.52037 Å, b = 4.52037 Å, c = 3.12181 Å, space grpup *P42/mnm*, R_{wp} = 5.05%, Chi2 = 6.58			

Table S4. Refined parameters of S–RuO_2/(F)C.

S–RuO_2/(F)C	X	Y	Z
Ru0	0.48556	0.51444	0.50000
Ru1	0.01766	-0.01766	-0.00000
O2	0.68746	0.69669	0.00000
O3	0.20040	0.79960	0.50000
O4	0.30330	0.31254	-0.00000
S1	0.80561	0.19439	0.50000
a = 4.48394 Å, b = 4.48394 Å, c = 3.11028 Å, space grpup *P42/mnm*, R_{wp} = 6.44%, Chi2 = 8.25			

Table S5. Refined parameters of P–RuO_2/(F)C.

P–RuO_2/(F)C	X	Y	Z
Ru0	0.48025	0.51975	0.50000
Ru1	0.02406	-0.02406	-0.00000
O2	0.68849	0.69716	0.00000
O3	0.19748	0.80252	0.50000
O4	0.30284	0.31151	-0.00000
P1	0.80241	0.19759	0.50000
a = 4.50192 Å, b = 4.50192 Å, c = 3.10770 Å, space grpup *P42/mnm*, R_{wp} = 4.53%, Chi2 = 3.74			

Table S6. Refined parameters of Se–RuO_2/(F)C.

Se–RuO_2/(F)C	X	Y	Z
Ru0	0.47722	0.52278	0.50000
Ru1	0.03359	-0.03359	0.00000
O2	0.68462	0.69946	-0.00000
O3	0.19975	0.80025	0.50000
O4	0.30055	0.31538	0.00000
Se1	0.80428	0.19572	0.50000
a = 4.49913 Å, b = 4.49913 Å, c = 3.10685 Å, space grpup *P42/mnm*, R_{wp} = 4.46%, Chi2 = 3.72			

Table S7. Refined parameters of Cl–RuO_2/(F)C.

Cl–RuO_2/(F)C	X	Y	Z
Ru0	0.47924	0.52077	0.50000
Ru1	0.02721	-0.02721	-0.00000
O2	0.68822	0.69910	0.00000
O3	0.19879	0.80120	0.50000
O4	0.30090	0.31178	-0.00000
Cl1	0.80563	0.19437	0.50000
a = 4.49933 Å, b = 4.49933 Å, c = 3.10890 Å, space grpup *P42/mnm*, R_{wp} = 6.20%, Chi2 = 6.45			

Table S8. Refined parameters of Br–RuO_2/(F)C.

Br–RuO_2/(F)C	X	Y	Z
Ru0	0.47220	0.52780	0.50000
Ru1	0.03881	-0.03881	-0.00000
O2	0.68573	0.70042	0.00000
O3	0.19902	0.80098	0.50000
O4	0.29958	0.31427	-0.00000
Br1	0.80468	0.19532	0.50000
a = 4.50267 Å, b = 4.50267 Å, c = 3.10783 Å, space grpup *P42/mnm*, R_{wp} = 4.78%, Chi2 = 3.56			

[41] Najarian, A. M. *et al.* Homomeric chains of intermolecular bonds scaffold octahedral germanium perovskites. *Nature* **620**, 328–335 (2023). **[Page 18, Line 11–12]**

3. Comment: The authors propose that the doping amount of F in RuO_2 is controlled by the annealing temperature. However, numerous studies have demonstrated that annealing temperature, even without any elemental doping, can significantly alter the intrinsic structure of RuO_2, such as the strength of Ru-O bonds and structural stability. These structural changes, in turn, influence both the catalytic activity and stability (Nat. Commun. 2025, 16, 801, DOI: 10.1038/s41467–025–56188–z). Therefore, the approach of using annealing temperature to control the F doping amount lacks sufficient rigor and needs further clarification.

[Author's Response]: Thanks for the valuable suggestion. According to the literature provided by the reviewers (*Nat. Commun.* **16**, 801 (2025)), the work of *Shao et al.* indicates that modulating the annealing temperature can induce a structural transformation in the electrocatalyst from amorphous (h–RuO_X) to highly crystalline RuO_2 (anh–RuO_2), thereby significantly enhancing its catalytic performance. Regrettably, although the heat treatment process substantially enhances the stability of anh–RuO_X (550 h@1 A cm^{-2}) relative to h–RuO_X (<1 min@ 1 A cm^{-2}), it still performs considerably worse than the F–RuO_2/FC (1440 h@1 A cm^{-2}) reported in our work (**Fig. 4e**).

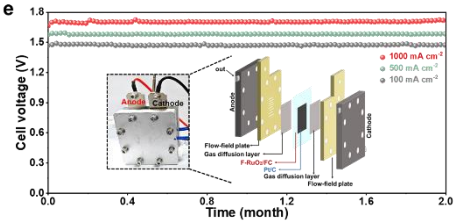

Figure 4. Electrochemical activity studies. (**e**) Chronopotentiometry tests of PEM electrolyzer using F–RuO_2/FC||Pt/C as electrocatalysts.

To investigate the influence of heat treatment temperature on the intrinsic structure of RuO_2 in this work, RuO_2(F)C was heat–treated at various temperatures (**Supplementary Fig. 67**). Evidently, a substantial difference in activity and stability exists between RuO_2(F)C and F–RuO_2/FC across various heat treatment temperatures, underscoring the impact of F–doping levels on stability. **[Page 10, Line 22–Page 11, Line 1]**

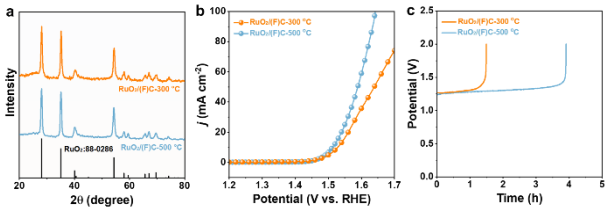

Supplementary Fig. 67. (**a**) XRD pattern, (**b**) OER polarization curve and (**c**) chronopotentiometry test of RuO_2/(F)C–300 °C and RuO_2/(F)C–500 °C.

Subsequently, we investigated the influence of heat treatment temperature on the F–doping level from multiple perspectives, as detailed below:

Firstly, F 1s XPS spectra were employed to further elucidate fluorine incorporation at various calcination temperatures (**Fig. 3b** and **Supplementary Fig. 51**). Obviously, the signal of Ru–F changed significantly with calcination temperature, indicating that the heat treatment process can indeed regulate the content of F.

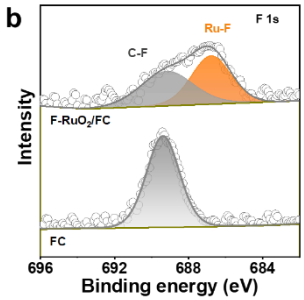

Figure 3. Electronic structure investigation. (**b**) F 1s XPS spectra of F–RuO_2/FC and FC.

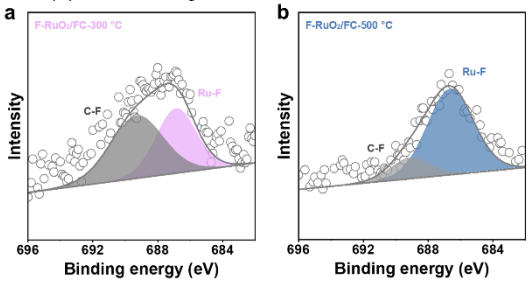

Supplementary Fig. 51. F 1s XPS spectra of (**a**) F–RuO_2/FC–300 °C and (**b**) F–RuO_2/FC–500 °C.

Secondly, EDS analysis indicates that the content of F in F–RuO_2/FC varies with the calcination temperature, which is consistent with the conclusion of XPS analysis (**Supplementary Fig. 50**).

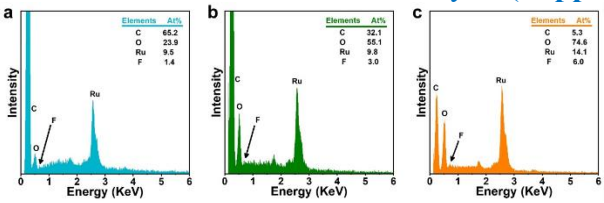

Supplementary Fig. 50. EDS spectra of (**a**) F–RuO_2/FC–300 °C, (**b**) F–RuO_2/FC, and (**c**) F–RuO_2/FC–500 °C.

Thirdly, Raman spectra were carried out in **Fig. 3a**, where the typical peaks at 506.8, 622.2, and 693.4 cm^{-1} are attributable to the vibration modes of E_g, A_{1g}, and B_{2g} for Ru–O bonds, respectively. Compared to RuO_2, a distinct red shift can be observed in the vibration peaks of F–RuO_2/FC at various calcination temperatures, which may be caused by the shortened Ru–O bond owing to the partial substitution of O by the highly electronegative F (**Supplementary Fig. 52**). [**Page 8, Line 22–Page 9, Line 1**]

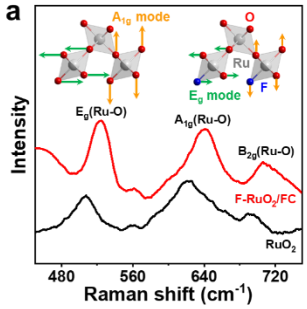

Figure 3. Electronic structure investigation. (**a**) Raman spectra of F–RuO_2/FC and RuO_2.

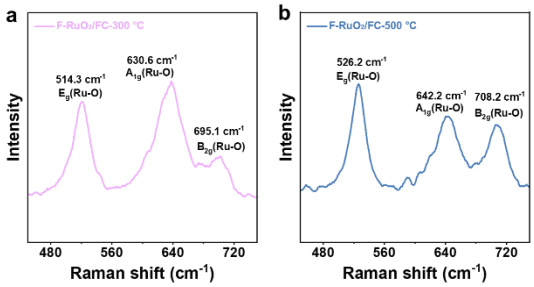

Supplementary Fig. 52. Raman spectra of (**a**) F–RuO_2/FC–300 °C and (**b**) F–RuO_2/FC–500 °C.

Finally, abundant literature also confirms that varying the annealing temperature allows for effective control over the content of incorporated non-metallic elements (*Nat. Nanotechnol.* **10**, 444–452 (2015); *Angew. Chem. Int. Ed.* **63**, e202412825 (2024)).
Based on the above analysis, controlling the annealing temperature can indeed affect the doping amount in RuO_2, thereby influencing the catalytic performance.

4. Comment: The newly added [Page 14, Lines 14–15] states: "Next, the ink was vertically dripped on the glassy carbon electrode (0.196 cm^2) to obtain the work electrode (loading amount: ~75 mg Ru)." The high loading of Ru seems to exaggerate the OER activity. A comparison with previous studies should be provided and summarized.
[Author's Response]: Thank you for pointing out this mistake, and we sincerely apologize for the oversight. The correct Ru loading amount on the working electrode (75 μg_{Ru} cm^{-2}) has been update in the electrochemical measurements section of the revised manuscript as following:

Electrochemical measurements. Then 2.0 mg of catalyst was added into the 200 μL of a solution containing 195 μL of isopropyl alcohol and 5 μL of Nafion, and the ink was prepared by ultrasonic at ambient temperature. Inductively coupled plasma atomic emission spectroscopy (ICP–AES) suggested that the content of Ru is 14.71 wt% (w_{Ru}). To prepare the working electrode, 10 μL of ink was vertically dripped on the glassy carbon electrode with a geometric area of 0.196 cm^2 (loading amount: ~75 μg_{Ru} cm^{-2}). [**Page 15, Line 3–8**]
In detail, the loading amount of Ru (m_{Ru}) on the working electrode was calculated by the following equation:

$$m_{Ru} = \frac{m_{loading} \times w_{Ru}}{S}$$

Where $m_{loading}$ is the mass of the catalyst dripped on the working electrode and S is the geometric area of glassy carbon electrode.

Therefore, the OER activities of overpotential and Tafel slope for various catalysts are visually presented in **Fig. 4a–c**, where F–RuO_2/FC exhibit the smallest overpotential and the Tafel slope value, outperforming most of the Ru–based catalysts reported recently (**Table S10**). [**Page 9, Line 22–Page 10, Line 6**]

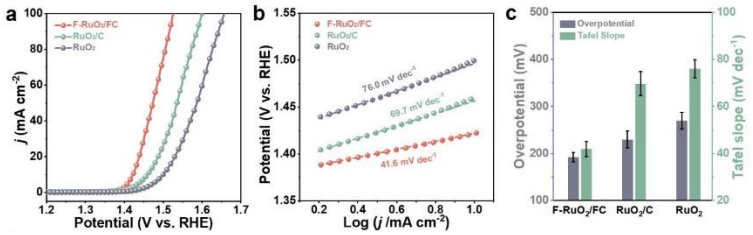

Figure 4. Electrochemical activity studies. (**a**) OER polarization curves and (**b**) Tafel plots of F–RuO_2/FC, RuO_2/C, and RuO_2. (**c**) Histogram of overpotentials at 10 mA cm^{-2} and Tafel slopes of F–RuO_2/FC, RuO_2/C, and RuO_2.

Table S10. Comparison of the Ru loading amount and OER performance of F–RuO_2/FC with recently reported OER electrocatalysts in a three–electrode setup.

Catalyst	Electrolyte	Loading amount of Ru	Activity (at 10 mA cm^{-2})	Tafel slope (mV dec^{-1})	Ref.
F–RuO_2/FC	**0.5 M H_2SO_4**	**75 μg cm^{-2}**	**192 mV**	**41.6**	**This work**
Pd@RuO_2	0.5 M H_2SO_4	200 μg cm^{-2}	189 mV	65.2	*J. Am. Chem. Soc.* **147**, 4159–4166 (2025)
GB–V–RuO_2	0.5 M H_2SO_4	697 μg cm^{-2}	159 mV	58.5	*Nat. Commun.* **16**, 4482 (2025)
Ru–γ–MnO_2	0.1 M $HClO_4$	12 μg cm^{-2}	246 mV	57.0	*J. Am. Chem. Soc.* **147**, 24392–24402 (2025)
RuO_2@COF–O(3)	0.5 M H_2SO_4	212 μg cm^{-2}	218 mV	64.3	*Adv. Mater.* **37**, 2417374 (2025)
Ga–RuO_2	0.5 M H_2SO_4	57 μg cm^{-2}	218 mV	60.5	*Angew. Chem. Int. Ed.* **137**, e202413334 (2025)
i$Ga_{0.2}Ru_{0.7}O_2$	1.0 M $HClO_4$	4000 μg cm^{-2}	188 mV	33.9	*Nat. Commun.* **16**, 3976 (2025)
h–ATO/RuO_2	0.5 M H_2SO_4	180 μg cm^{-2}	216 mV	60.0	*Nat. Commun.* **16**, 337 (2025)
RuFe@CF	0.5 M H_2SO_4	823 μg cm^{-2}	188 mV	80.3	*Adv. Mater.* **36**, 2312369 (2024)
Ir–RuO_2	0.5 M H_2SO_4	625 μg cm^{-2}	167 mV	48.2	*Nat. Commun.* **15**, 10315 (2024)
In$SnRuO_2$	0.5 M H_2SO_4	200 μg cm^{-2}	183 mV	49.8	*Adv. Mater.* **36**, 2414579 (2024)
Pb–RuO_2	0.5 M H_2SO_4	436 μg cm^{-2}	188 mV	58.6	*Nat. Commun.* **15**, 9774 (2024)
M–$RuIrFeCoNiO_2$	0.5 M H_2SO_4	1377 μg cm^{-2}	189 mV	49.0	*Sci. Adv.* **9**, eadf9144 (2023)
Ru/TiO_X	0.5 M H_2SO_4	71 μg cm^{-2}	174 mV	45.6	*Nat. Commun.* **14**, 7644 (2023)
$SnRuO_X$	0.5 M H_2SO_4	15 μg cm^{-2}	194 mV	38.2	*Nat. Commun.* **14**, 843 (2023)
$Li_{0.52}RuO_2$	0.5 M H_2SO_4	637 μg cm^{-2}	156 mV	83.3	*Nat. Commun.* **13**, 3784 (2022)
C–RuO_2–RuSe–5	0.5 M H_2SO_4	306 μg cm^{-2}	212 mV	49.5	*Chem* **8**, 1673–1687 (2022)
RuO_2–WC NPs	0.5 M H_2SO_4	22 μg cm^{-2}	347 mV	75.7	*Angew. Chem. Int. Ed.* **61**, e202202519 (2022)
SS Pt–RuO_2 HNSs	0.5 M H_2SO_4	306 μg cm^{-2}	260 mV	51.0	*Sci. Adv.* **8**, eabl9271 (2022)

5. Comment: Additional, [Page 14, Lines 9–12]: "In addition, melamine, …… at 450 °C, 150 °C, 300 °C, 500 °C, 450 °C, and 350 °C, respectively". The repetition of 450 °C appears to be an error. Such inconsistencies may undermine the rigor of the manuscript.

[Author's Response]: Thank you for your thorough review of our manuscript. To address your concern, we have further clarified and elaborated on the synthesis process for the M–RuO_2/(F)C (M = N, S, P, Se, Cl and Br) electrocatalyst in the revised manuscript. As shown in **Supplementary Fig. 80**, the anion sources and RuO_2/(F)C were placed in separate tube furnaces located upstream and downstream of the quartz tube for heat treatment. This configuration facilitates sufficient anion release from the anion sources at different target temperatures (**Table S12**). [**Page 14, Line 16–Page 15, Line 1**]

Supplementary Fig. 80. Schematic diagram of the heat treatment synthesis process for M–RuO_2/(F)C (M = N, S, P, Se, Cl and Br) using tube furnace.

Table S12. Target temperature under heat treatment of different anion sources.

Anion sources	Target temperature (°C)
melamine	450
sulfur powder	150
sodium hypophosphite	300
selenium powder	500
a mixture of polyvinyl chloride and manganese dioxide	450
hexabromobenzene	350

6. Comment: The PEM tests lack control samples (RuO_2, RuO_2/(F)C) for comparison, which are crucial for enabling readers to more effectively assess the catalytic performance.

[Author's Response]: We sincerely appreciate your insightful feedback, as it has provided important guidance for enhancing our work. According to your suggestion, RuO_2 and RuO_2/(F)C were employed as anode catalysts for the PEM electrolyzer, and their respective electrochemical performances were systematically evaluated. Specifically, to deliver current densities of 500, 1000, 2000, and 3000 mA cm^{-2}, higher cell voltages of RuO_2||PEM||Pt/C (1.61, 1.78, 2.10 and 2.42 V) and RuO_2/(F)C||PEM||Pt/C (1.70, 1.96, 2.44 and 2.86 V) were required compare with F–RuO_2/FC (1.58, 1.70, 1.89 and 2.05 V) (**Supplementary Fig. 70a**). Notably, both RuO_2||PEM||Pt/C and RuO_2/(F)C||PEM||Pt/C exhibit significantly lower stability than that of F–RuO_2/FC, and the severe degradation of RuO_2/(F)C underscores the pivotal role of F in catalytic stability (**Supplementary Fig. 70b, c** and **Supplementary Fig. 71**). [**Page 11, Line 8–16**]

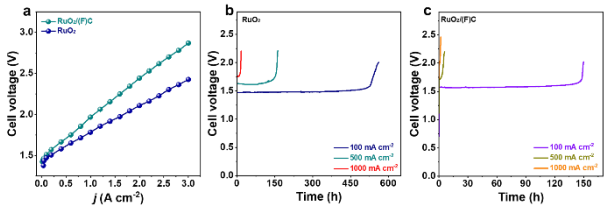

Supplementary Fig. 70. (**a**) Polarization curves of PEM electrolyzer using RuO_2/(F)C and RuO_2 as anode. Chronopotentiometry tests of PEM electrolyzer using (b) RuO_2||Pt/C and (c) RuO_2/(F)C||Pt/C as electrocatalysts.

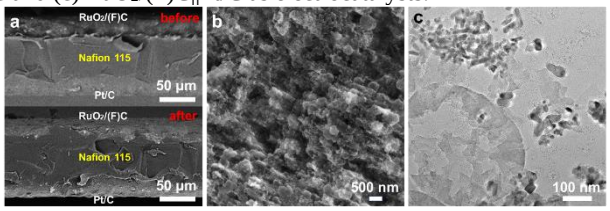

Supplementary Fig. 71. (**a**) SEM images of the cross section of MEA before and after CP test. (**b**) SEM image and (**c**) TEM image of RuO_2/(F)C after CP test of PEMWE.

General comment: In summary, this manuscript does not provide sufficient evidence to demonstrate clear differences in the degree of symmetry breaking across various anionic dopants. Therefore, this work far can not meet the high standards of Nature Communications.

[Author's Response]: Thank you very much for your constructive comments. We highly appreciate that you strictly point out our deficiency in this work and we are truly sorry that our work did not supply a satisfying interpretation and explanation to demonstrate our research. To address your concerns, we have, according to the literature (*Nature* **620**, 328–335 (2023)), employed the Baur distortion index to quantify the observed differences in the degree of symmetry breaking among the various anionic dopants.

In the end, we would like to thank for the precious time of the reviewers and the editor. We sincerely wish that our point-to-point response and the revised manuscript have addressed your concerns and satisfy your requirements for publications. We would be grateful if we have the chance to share our work with readers of ***Nature Communications***.

Xiaoqing Huang

Response to Reviewers

Dear Reviewer,

Thank you for your continued guidance and the valuable time you have dedicated to our manuscript titled **"Ultradurable acidic water oxidation ruthenium–based electrocatalyst by fluorination induced symmetry–breaking"** (**Manuscript ID: NCOMMS-25-10822B-Z**) for ***Nature Communications***. We are greatly encouraged by your positive recognition of our previous revisions. Regarding the final point raised, we have given it in-depth consideration and provided a detailed explanation below. We sincerely hope these revisions have adequately addressed your concern and further improved the quality of the manuscript.

Reviewer #1

1. Comment: In the revised manuscript, the authors have made efforts to improve the quality of the presented research. However, the reviewer raises a final concern regarding how to distinguish the effects of doping amount from the type of doping element on the Baur distortion indices.

[Author's Response]: Thank you for acknowledging our efforts in previous revisions and for raising this critical concern about attributing the distinction between the effects of dopant type and doping amount on the Baur distortion indices (D_i). We fully agree that addressing this point is essential to solidify the scientific rigor of our conclusions. Motivated by this question, we conducted an in–depth investigation. It was revealed that the type of doping element is the key factor driving the change of D_i, whereas the doping amount modulates the OER performance mainly through affecting the number of active sites and D_i. This conclusion is drawn from the following analysis:

The effect of doping element type: Evidently, M–RuO_2 (M = F, N, S, P, Se, Cl and Br) shows varying D_i values at comparable doping levels (**Supplementary Fig. 46, 52b,** and **47**), demonstrating that the doping element type critically determines the D_i.

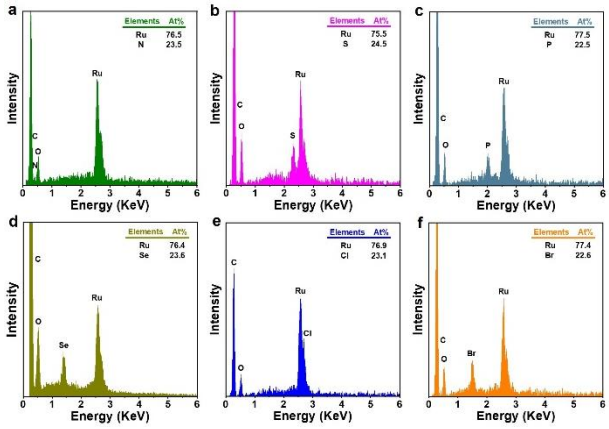

Supplementary Fig. 46. EDS spectra of (**a**) N–RuO_2/(F)C, (**b**) S–RuO_2/(F)C, (**c**) P–RuO_2/(F)C, (**d**) Se–RuO_2/(F)C, (**e**) Cl–RuO_2/(F)C and (**f**) Br–RuO_2/(F)C.

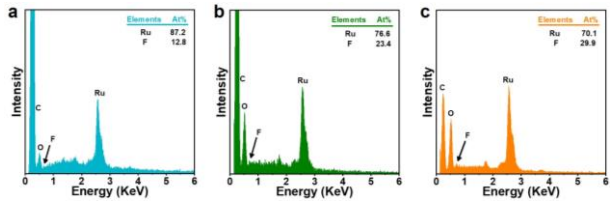

Supplementary Fig. 52. EDS spectra of (**a**) F–RuO_2/FC–300 °C, (**b**) F–RuO_2/FC, and (**c**) F–RuO_2/FC–500 °C.

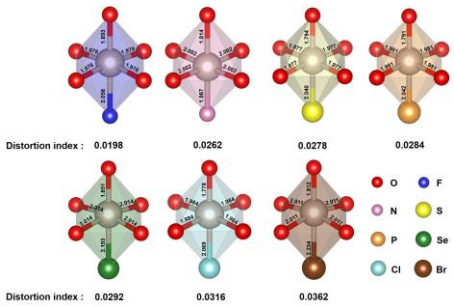

Supplementary Fig. 47. The metal–nonmetal bond length of F–RuO_2, N–RuO_2, S–RuO_2, P–RuO_2, Se–RuO_2, Cl–RuO_2 and Br–RuO_2 crystal structure. The calculated distortion indexes are indicated.

The effect of doping amount: Taking F doping as an example, at low doping levels (**Supplementary Fig. 52a**), the D_i remains largely unchanged (**Supplementary Fig. 50a, 51a,** and **Table S9**), while the TOF decreases significantly (**Supplementary Fig. 64**), suggesting that low F doping primarily affects the number of active sites rather than the D_i. Conversely, as the F doping levels increase (**Supplementary Fig. 52c**), D_i increases while TOF decreases (**Supplementary Fig. 50b, 51b, 64** and **Table S10**), demonstrating that excessive symmetry breaking degrades OER performance (**Supplementary Fig. 63**) [**Page 10, Line 20–Page 11, Line 1**].

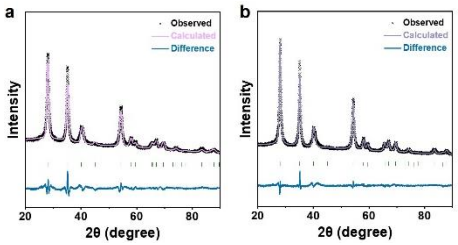

Supplementary Fig. 50. XRD patterns of (**a**) F–RuO_2/FC–300 °C and (**b**) F–RuO_2/FC–500 °C.

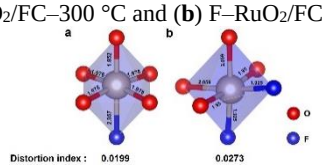

Supplementary Fig. 51. The metal–nonmetal bond length of (**a**) F–RuO_2/FC–300 °C and (**b**) F–RuO_2/FC–500 °C crystal structure. The calculated distortion indexes are indicated.

Table S9. Refined parameters of F–RuO_2/FC–300 °C.

F–RuO_2/FC–300 °C	X	Y	Z
Ru0	0.48485	0.51515	0.50000
Ru1	0.01696	-0.01656	0.00000
O2	0.69389	0.69616	0.00000
O3	0.19322	0.80779	0.50000
O4	0.30384	0.30611	-0.00000
F1	0.80894	0.19002	0.50000
a = 4.48250 Å, b = 4.48250 Å, c = 3.11133 Å, space grpup *P42/mnm*, R_{wp} = 5.16%, Chi2 = 7.36			

Table S10. Refined parameters of F–RuO_2/FC–500 °C.

F–RuO_2/FC–500 °C	X	Y	Z
Ru0	0.48580	0.48576	0.50000
Ru1	0.01298	0.01297	0.00000
O2	0.69602	0.69649	0.00000
O3	0.19388	0.80445	0.50000
O4	0.80428	0.19361	0.50000
F1	0.30704	0.30674	0.00000
F2	0.30679	0.30661	0.00000
a = 4.48250 Å, b = 4.48250 Å, c = 3.12181 Å, space grpup *P42/mnm*, R_{wp} = 4.32%, Chi2 = 2.95			

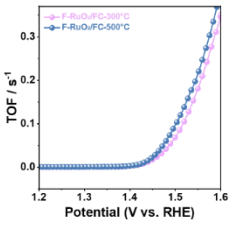

Supplementary Fig. 64. TOF of F–RuO_2/FC–300 °C and F–RuO_2/FC–500 °C.

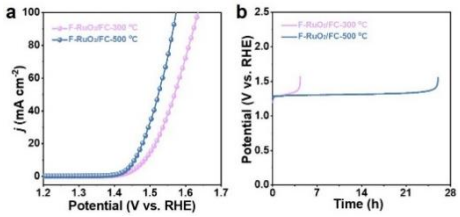

Supplementary Fig. 63. (**a**) OER polarization curves and (**b**) chronopotentiometry tests of F–RuO_2/FC–300 °C and F–RuO_2/FC–500 °C.

In the end, we extend our sincere appreciation to the editor and reviewers for the precious time and the valuable feedback throughout the review process. We sincerely wish that the revised manuscript and our response have adequately addressed your concerns and meet the high standards for publication. We would be grateful if we have the chance to share our work with readers of ***Nature Communications***.

Xiaoqing Huang